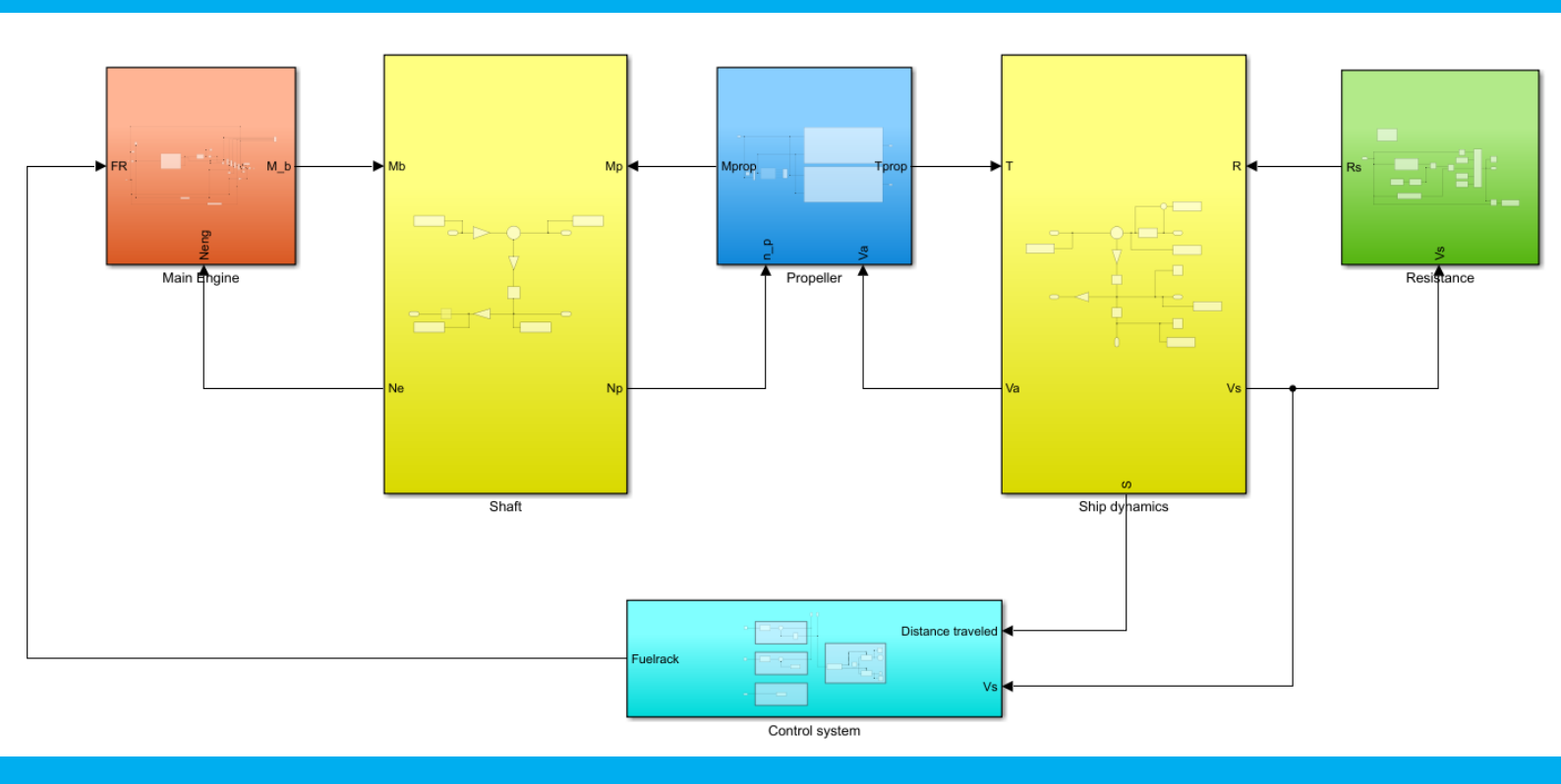
Voyage simulation of a post-Panamax container ship sailing on ammoniadiesel or hydrogendiesel fuel

W. van Dijk





Voyage simulation of a post-Panamax container ship sailing on ammonia-diesel or hydrogen-diesel fuel

by

W. van Dijk

to obtain the degree of Master of Science at the Delft University of Technology, to be defended publicly on Thursday October 30, 2025 at 13:30 AM.

MT.25/26.007.M

Student number: 5088615

Project duration: September 24, 2024 – October 30, 2025 Thesis committee: Dr. ir. P. de Vos TU Delft, supervisor

Dr. M. Merts MARIN Ir. X. Jiang TU Delft



Preface

This thesis represents the culmination of my master's research at Delft University of Technology. It investigates the modeling and simulation of a post-Panamax container ship operating on dual-fuel configurations: diesel-ammonia and diesel-hydrogen. The study was conducted within the framework of the AmmoniaDrive project, which aims to explore cleaner fuel alternatives for the maritime sector.

I am grateful to my supervisor, dr. ir. P. de Vos, for his invaluable guidance, patience, and encouragement throughout the process. I also wish to thank dr. M. Merts of MARIN for his feedback and technical insights. My colleagues and peers at TU Delft provided a stimulating environment for research and discussion, for which I am sincerely appreciative.

Finally, I would like to express my heartfelt gratitude to my family and friends for their unwavering support during this demanding journey.

W. van Dijk Delft, October 2025

The author acknowledges the use of Al-based writing assistance tools to support grammar checking, language refinement, and small stylistic improvements. These tools were not used to generate original content, analyses, or conclusions presented in this thesis.

Abstract

The maritime industry faces growing pressure to reduce greenhouse gas (GHG) emissions and transition toward sustainable propulsion technologies. This thesis investigates the feasibility of employing ammonia and hydrogen as alternative fuels in dual-fuel configurations with diesel for large two-stroke internal combustion engines (ICEs). A voyage simulation model of a post-Panamax container ship (the Duisburg Testcase) was developed in MATLAB Simulink to evaluate fuel performance under voyage conditions.

The research includes a review of the properties of ammonia and hydrogen, the development of dual-fuel engine models based on the Seiliger process, and the integration of these models into a time-domain voyage simulator. Simulations were performed for diesel, diesel—ammonia, and diesel—hydrogen operation to compare fuel consumption and efficiency.

Results show that both ammonia and hydrogen can be more energy efficient relative to conventional diesel operation. Ammonia offers promising scalability and easier storage, while hydrogen achieves higher efficiency but presents greater challenges regarding storage and safety. The developed simulation framework provides a tool for evaluating and optimizing dual-fuel propulsion systems, supporting the maritime sector's transition to cleaner energy solutions.

Table of Contents

P	eface	i
A	stract	ii
Т	ole of Contents i	iv
L	et of figures	vi
	-	rii
	menclature vi	
1	Introduction	1
Liter	ture review	3
2	2.1 Ammonia as fuel	4 4 6 7
3		8 8 8
4	On Combustion Engine models 1 4.1 Varying models 1 4.2 Seiliger modeling 1 4.3 Friction modeling 1 4.4 Section conclusion 1	1 2
5	On dual-fuel engine models 1 5.1 Model of Dual-fuel engine model 1 5.2 Ammonia 1 5.3 Hydrogen 1 5.4 Section conclusion 1	4 6
Rese	rch 1	8
6	Voyage simulator16.1 Resistance26.2 Propeller26.3 Wake fraction and Thrust deduction26.4 Ship and Shaft dynamics implementation26.5 Internal Combustion Engine26.6 Control systems2	21 22 22 23

Table of Contents iv

7	Intermediate results 7.1 Model results	29
	Alternative fuels model integration 8.1 Ammonia limitations in literature	35
9	Results9.1 Diesel-Ammonia9.2 Diesel-Hydrogen9.3 Case study (continuation)	40
10	Conclusion	44
11	Discussion and recommendations	45
Α	Simulink implementation and code	49
В	Simulator Results	55

List of Figures

1.1	AmmoniaDrive preliminary system lay-out (De Vos, 2020)	1
4.1	Example of a Seiliger cycle (based on the formulas in Stapersma (2010))	11
5.1	Measured engine BSFC data for respective fuels under constant power output operation using various combinations of ammonia/diesel fuel. (Reiter & Kong, 2010)	14
5.2	Heat release rate of ammonia-diesel combustion at constant ammonia energy ratio at varying loads. (Cui & Wang, 2023)	15
5.3	Heat balance under different diesel energy fraction for the HPDF mode. (X. Zhou et al., 2022)	16
6.1	Simulink model layout	19
6.2	Wave resistance coefficient as a function of the full scale vessel with trend line	21
6.3	Openwater diagram from the available data from the Duisburg Test Case	22
6.4	Visualization of the energy losses in an ICE (Woud & Stapersma, 2002)	26
6.5	Simulink control system	27
7.1	Resistance results from Simulink	28
7.2	Open-water diagram for the propeller as implemented in Simulink	29
7.3	Inlet pressure as function of available turbo heat ($c_{tc} = 0.06$)	29
7.4	Sailing speed for diesel in the case study	30
7.5	P-V diagrams for different engine loads with Diesel fuel	30 31
7.6 7.7	Energy and fuel consumption of the diesel model in the case study	31
1.1	Efficiencies of the dieser engine as a function of Fuer Nack	31
8.1	Simulation data from X. Zhou et al. (2022) shows the heat balance for different diesel	
0 0	energy percentages at constant engine speed and injected fuel energy	32
8.2 8.3	Combustion efficiency based on X. Zhou et al. (2022)	33
0.3	losses where energy does not work in the cylinder process	33
8.4	Illustration of the data processing, where data is extracted from a figure and processes	55
0	into the total heat energy injected	33
8.5	Heat Division parameter as a function of Engine load	34
8.6	Heat Division parameter as a function of Engine speed	34
8.7	Heat division as a function of fuel rack and normalized engine speed derived with data	
	from Cui and Wang (2023)	34
8.8	Changes to Simulink to incorporate the ammonia mixture	36
8.9	Changes to Simulink to incorporate the hydrogen mixture	36
	AER as function of Fuel rack	37
8.11	HER as function of Fuel rack	37
9.1	Heat input efficiency as function of fuel rack position	38
9.2	Thermodynamic efficiency as function of engine speed and fuel rack position	39
9.3	Engine efficiency as function of engine speed and fuel rack position	39
9.4	Engine efficiencies as functions of different parameters under propeller load	40

List of Figures vi

9.5	P-V diagram for different engine loads with Diesel-Ammonia fuel	40
9.6	Heat division parameter <i>X</i> as function of the engine speed	41
9.7	Combustion efficiency η_{cb} and heat input efficiency η_q as a function of engine speed	41
9.8	Engine efficiencies as functions of different parameters under accelerating propeller load	41
9.9	P-V diagram for different engine loads with Diesel-Hydrogen fuel	41
9.10	Voyage results for the different fuel configurations	42
	Fuel consumption results for the voyage	43
9.12	Total Energy flow for all three fuel-mixtures	43
	Simulink model layout	49
	Simulink Resistance block	49
	Simulink propeller block	50
A.4	Simulink Ship block	50
A.5	Simulink Shaft block	51
A.6	Simulink control system	51
A.7	Engine implementation in Simulink	52
A.8	Seiliger implementation in Simulink	52
	Cylinder heat input model with heat input, combustion and cooling losses and heat division	
	Implementation of the thermodynamic formulas for isentropic compression	53
	Implementation of the thermodynamic formulas for isochoric combustion	53
	Implementation of the thermodynamic formulas for isobaric combustion	54
A.13	Implementation of the thermodynamic formulas for isentropic expansion	54
A.14	Turbo model	54
	Fuel mass flow, Energy flow and Fuel mass consumed for the Diesel voyage simulation	55
B.2	Fuel mass flow, Energy flow and Fuel mass consumed for the Diesel-Ammonia voyage	
	simulation	56
B.3	Fuel mass flow, Energy flow and Fuel mass consumed for the Diesel-Hydrogen voyage	
	simulation	57

List of Tables

	Properties of different fuels in the marine industry	4
2.2	Advantages and disadvantages of ammonia as a energy source (derived from Lesmana et al. (2019))	5
2.3	Advantages and disadvantages of hydrogen as a energy source. (summary of section 2.2)	7
4.1	Main characteristics of the different modeling techniques (Alberer et al., 2011)	11
5.1	Engine data used by Cui and Wang (2023)	15
6.2	Resistance data from the Duisburg model tests	21
7.2	Engine Data from WinGD (2024)	30
8.1	Engine data used by Cui and Wang (2023)	33

Nomenclature

Abbreviations

(B)SFC (Break) Specific Fuel Consumption

AER Ammonia Energy Ratio
AMR Ammonia Mass Ratio
BDC Bottom Dead Center

CFD Computational Fluid Dynamics

CO Carbon mono-oxide CO2 Carbon dioxide

E&FM Emptying-and-Filling Model EGR Exhaust Gas Recycling

FR Fuel Rack

GHG Green house gas H2 Hydrogen gas

HER Hydrogen Energy Ratio
HHV Higher Heating Value
HMR Hydrogen Mass Ratio
HPDF High Pressure Dual Fuel
ICE Internal combustion engine

IDT Initial Delay Time

LES Large Eddies Simulation
LHV Lower Heating Value
LSHFO Low sulfur heavy fuel oil
MDO Marine Diesel Oil

MVM Mean Value Model Nox Nitrous oxides

RANS Reynolds-Averaged Navier-Stokes SCR Selective Catalistic Reduction

SM Sea Margin

SOFC Solid Oxide Fuel cell TDC Top Dead Center WAM Wave Action Model List of Tables ix

Symbols

σ	Stoichiometric air fuel ratio	kg/kg
С	Coefficient	-
C_p	Heat capacity at constant pressure	kJ/(kgK)
C_v	Heat capacity at constant volume	kJ/(kgK)
D	Diameter	m
γ	cp/cv	-
h_L	Lower heating value	MJ/kg
k	Form factor	-
K_Q	Non dimensional coefficient Torque	-
K_T	Non dimensional coefficient Thrust	-
Μ	Torque	Nm
n	Rotary speed	RPM/RPS
ν	Specific volume	m³/kg
P	Power	W
p	Pressure	Pa
q	Specific heat	J
Q	Heat	J
R	Resistance	(k)N
R	Ratio	-
Re	Reynolds number	_
ρ	Density	kg/m³
S	Surface	m^2
t	Thrust deduction factor	-
T	Temperature	K
v	Speed	m/s
W	Wake fraction	-
W	Work	J/kg
W	Specific work	J/kg
X	Heat division parameter	-

Subscribs

advance а air а b brake С compression comb combustion constant pressure ср constant volume CV engine е expansion е friction f f fuel indicated model m mechanical m propeller р ship s Τ total wave W W wet

List of Tables x

Efficiencies

 $\begin{array}{ll} \eta_{comb} & \text{combustion efficiency} \\ \eta_e & \text{engine efficiency} \\ \eta_h & \text{hull efficiency} \\ \eta_q & \text{heat input efficiency} \\ \eta_m & \text{mechanical efficiency} \\ \eta_o & \text{open water efficiency} \\ \eta_{td} & \text{thermodynamic efficiency} \end{array}$

Chapter 1

Introduction

The maritime sector is under increasing pressure to reduce greenhouse gas (GHG) emissions and transition towards cleaner propulsion technologies. Among the potential solutions, ammonia and hydrogen are considered promising alternative fuels. Ammonia offers favorable storage conditions and can serve as a hydrogen carrier, while hydrogen provides high gravimetric energy density and zero carbon emissions. Both fuels, however, present challenges in combustion, safety, and infrastructure that require thorough investigation.

The use of ammonia as a fuel is not new. It was briefly adopted during World War II due to oil shortages, with notable applications such as Belgian buses operating on ammonia. After the war, low-cost oil-based fuels displaced ammonia. Today, the urgency of decarbonization has renewed interest in ammonia, notably through initiatives such as the AmmoniaDrive project (De Vos, 2020), which explores its role as a hydrogen and energy carrier.

While solid oxide fuel cells (SOFCs) have been studied as part of this project, the maritime industry still primarily relies on large two-stroke internal combustion engines (ICEs) for propulsion (Stapersma, 2010, p. 14). Therefore, this thesis focuses on the ICE pathway, specifically on the modeling and simulation of a dual-fuel system capable of operating on diesel, diesel—ammonia, and diesel—hydrogen mixtures. The Duisburg Testcase vessel (Moctar et al., 2012), with extensive towing tank data available, serves as the simulation vessel.

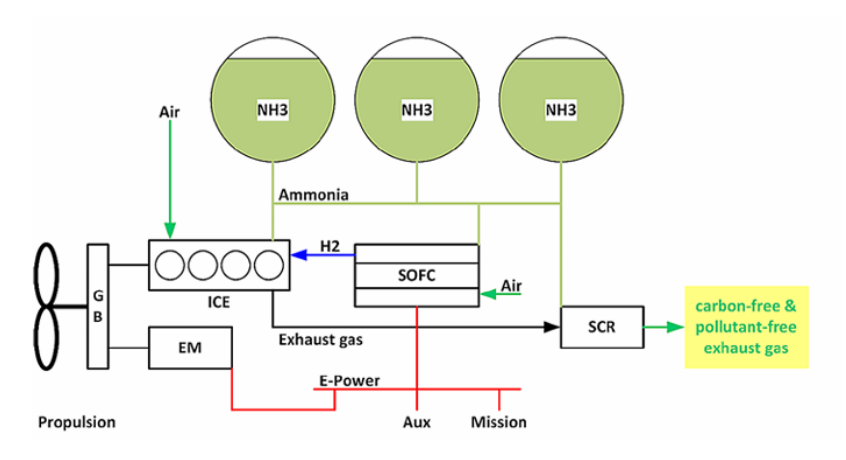


Figure 1.1: AmmoniaDrive preliminary system lay-out (De Vos, 2020)

Research questions

The main research question for this MSc project is presented below. The question will be answered by breaking it into sub-questions.

How can an ICE be modeled to use diesel, diesel-ammonia, and diesel-hydrogen to show the effects of these fuels in voyage simulations?

To formulate a methodology for the research question, sub-questions for a literature review have been created:

- 1. Why use ammonia and hydrogen as fuel in internal combustion engines?
- 2. How are engine models used in time domain models for voyage simulations?
- 3. How can different internal combustion engine models be used to model the use of conventional diesel fuel?
- 4. How can dual-fuel combustion be modeled with ammonia and hydrogen?
- 5. What research gap exists in the time domain simulation of ICE's with respect to the alternative fuels?

For breaking down the research part, the following sub-questions were created.

- 1. How can the hydrodynamic part and the ICE of the simulation be modeled?
- 2. How can the influence of ammonia be modeled for the simulator?
- 3. How can hydrogen literature be applied for the simulator?

Literature review

Chapter 2

On alternative fuels

This section of the literature review will focus on the first sub-question:

Why use ammonia and hydrogen in internal combustion engines?

When different fuels are considered, the properties of these fuels are an important factor to take into account. Table 2.1 by Di Blasio et al. (2021) lists these properties which will be examined in further detail. Di Blasio et al. compiled a summary of common marine fuels such as MDO and LSHFO, as well as cleaner alternatives. This literature review will focus only on the use of ammonia and hydrogen. Ammonia as fuel will be discussed in Section 2.1 and hydrogen in Section 2.2.

Properties	MDO	LSHFO	Ammonia	Hydrogen (gaseous/liquid)
Chemical formula	C_{10} - C_{15}	C ₈ -C ₂₅	NH_3	H_2
Auto-ignition temperature (°C)	210	230	651	571-585
Latent heat of vaporization (kJ/kg)	47.86	~47.86	1 369	0/NA
Lower heating value (MJ/kg)	43.5	~43.5	18.5	120.1
Flammability limits in air (Vol%)	0.6-7.5	0.6-7.5	16-25	4.0-75
Flame speed (cm/s)	87	~87	14	270
Fuel density (kg/m³)	796-841	975-1 010	602.8	17.5/71.0
Energy density (MJ/m³)	36 403	~36 403	11 333	2 101/8 539
Storage method	Liquid	Liquid	Comp. liquid	Comp. gas /cry. liquid
Storage temperature (°C)	25	25	25	25/-253
Storage pressure (bar)	1	1	10	248/1

Table 2.1: Properties of different fuels in the marine industry

2.1 Ammonia as fuel

Ammonia as a fuel has different advantages and disadvantages as listed below by Lesmana et al. (2019) and summarized in Table 2.2. The strengths of ammonia are the relative high energy density both gravimetric and volumetric when compared to hydrogen, meaning less fuel has to be stored on the ship for sailing. Another listed positive point is the anti-knock quality reducing knock, which lowers efficiency and can be damaging to an engine. Ammonia also has favorable storage properties, because it can be stored as a compressed liquid with a low pressure of 10 bar and without cryogenic equipment. This in comparison to hydrogen, which requires high storage pressures or extremely cold storage. The

2.1. Ammonia as fuel 5

last listed advantages of ammonia is the fact that ammonia combustion does not lead to direct \mathcal{CO}_2 emissions as there is no carbon-bonds in the fuel.

The use of ammonia also has obstacles to be considered: The first is the high latent heat of vaporization as shown in Table 2.1. After the compression stage, the temperature is high enough for the MDO to evaporate and combust. However, ammonia has a much larger latent heat of vaporization, resulting in a cooling effect that requires alternatives to the use of only ammonia (Lesmana et al., 2019). Lewandowski et al. (2023) found that the temperature drop at TDC can be 130 K with a pressure drop 3-4 bar.

Another issue is the high ignition temperature (when compared to conventional fuels) as shown in Table 2.1. The high ignition temperature makes the fuel harder to combust and can lead to an increased initial delay time (IDT). Different recent research (Song et al., 2024) has been conducted to determine the characteristics of ammonia combustion with a pilot fuel. The research also focused on optimizing the IDT in terms of percentage pilot fuel, which resulted in a way to predict the IDT.

Another aspect of ammonia is its cleaning power and use in cleaning products. This can raise questions about whether the lubrication can be removed while using ammonia. Although Coppo (2023) focuses primarily on the design of an injector capable of injecting ammonia researched, they also did research on the corrosion as a result of degreasing with ammonia. In the experiment, they kept the different materials in ammonia fuel, after which they concluded that no corrosion had occurred as long as the materials were continuously immersed in fuel. Alternatively, the corrosive aspect is looked into in Reiter and Kong (2010), where the authors note that no real influence has been found.

Fuel bound nitrogen will cause nitrogen oxide emission to form after combustion. However, with recent progress in the development and use of selective catalytic reduction (SCR) (as reported by J. Zhou and Wang (2020)), NOx emissions are less important to consider as they can be lowered with this technology.

Another area of focus is the evaluation of the feasibility and safety of ammonia. Both aspects are covered by De Vries (2019). The author considers different ways of using ammonia as a fuel such as fuel cells and internal combustion engines. De Vries concludes that the use of an ICE is the efficient way to utilize ammonia after an SOFC. However the ICE is more reliable and less expensive. From a cost perspective, an ammonia ICE would be about 3.2 times the expenses of the conventional fuels based on data available in 2019. De Vries also looked into the safety aspect of the alternative fuel. In terms of flammability and ignition, the author does not note significant concerns as ammonia requires a large and narrow amount in the air before it becomes flammable (see Table 2.1). When looking at toxicity for the marine environment, there are also no significant concerns as ammonia is a part of the nitrogen cycle. Of course, spillage must be as small as possible. However, for humans, ammonia is very toxic, so detection and ventilation should be used to minimize risks.

Table 2.2: Advantages and	disadvantages of ammonia a	as a energy source (derived from	Lesmana et al. (2019)).

Advantages	Disadvantages
High energy density when compared to other	High latent heat of vaporization resulting in more
alternative fuels	heat absorption
Relatively high LHV and HHV on the basis of	Low flame speed resulting in low combustion efficiency
unit mass	and incomplete combustion at higher engine speeds
High octane number resulting in good anti-knock	High auto-ignition temperature being troublesome
qualities	in compression ignition engines
Easy handling and storage	Narrow flammability limit increasing change of
Lasy Hariuming and Storage	misfire in lean or rich conditions
No carbon based emissions	NOx emission by fuel bound nitrogen

2.2 Hydrogen as fuel

Another alternative fuel considered is hydrogen. As a fuel, hydrogen, as ammonia, has the advantage of no fuel-bound carbons. The combustion will not result in CO_2 emissions. Hydrogen can be used as a fuel in different ways. The first method, which is not further considered in this literature review, is fuel cells. Fuel cells, which are very efficient, have the cost disadvantage compared to ICE (Dere, 2023). A second advantage is the high gravimetric energy density (Table 2.1), which is higher than conventional diesel. However, this also depends on the storage method and also brings a disadvantage, as will be explained later.

The first disadvantage of hydrogen is predicted by El-Gohary (2009). The combustion of hydrogen occurs very fast, resulting in high peak temperatures. This also leads to high heat losses, lowering the overall efficiency of the engine. In addition, lower break mean effective pressure is available when compared to a diesel engine. This means a larger engine will be required to reach the required power. The high temperature also leads to NOx emissions, which is a limit to engine performance (Kumar Agarwal & Valera, 2021).

Hydrogen has, as ammonia, a high auto-ignition temperature (Table 2.1). This makes it difficult to initiate the combustion on only temperature (Kumar Agarwal & Valera, 2021). Therefore, using a pilot fuel to start the ignition can be considered to increase the performance. This will be explored in more detail in Section 5.

When looking at storage on a ship, there are four main options, as summarized by Seddiek et al. (2015). The first method is compressed hydrogen storage, in which hydrogen is stored as a gas at a pressure of 350 to 700 bar. Although the setup is the simplest to realize (requiring only a compressor and pressure tank), the disadvantage is the low energy density of the hydrogen from a volumetric view. This can be seen in Table 2.1. Also costs will increase with a greater storage pressure, while a pressure increase will increase the energy density. The safety of pressurized hydrogen can also become a danger if a rupture occurs in the tank. As investigated by Li et al. (2022), hydrogen jets can spontaneously combust when leaking occurs. The second option is the storage of liquefied hydrogen. However, storing hydrogen as a liquid requires cryogenic equipment, as the temperature of liquid hydrogen is -253 °C. This method will increase the energy density of the fuel and make implementation more viable.

The third option is to use metal hydrides. Metal hydride binds the hydrogen to its surface and releases heat. When hydrogen needs to be used, heat can be added back to undo the bonds and released back into the air. No hydrogen leakage can occur when no heat is added, so this storage method is possible very safe (Kumar Agarwal & Valera, 2021). The drawbacks of this technology are that more research is required to determine if it is applicable on a large scale (Ley et al., 2014). A more fundamental issue is that as hydrogen fuel is used, the metal remains and has to be taken as a useless weight. In contrast, transporting hydrogen gas in tanks, where after combustion no materials remain. The last method of storing hydrogen is through other hydrogen carriers. An example is ammonia, which can be used directly as fuel as explored in Section 2.1 or cracked back into hydrogen.

Other dangers of hydrogen are the high explosion limits in air as the mixture becomes explosive between 4-75

Vol % (Table 2.1). Small leaks become dangerous quickly and require ventilation in the storage space. Material failure can also become a problem. As explained in Li et al. (2022), 3 mechanisms can occur: Hydrogen embrittlement (hydrogen reactions changing the material structure), hydrogen-induced cracking (hydrogen pressure building in internal cracks), and high temperature hydrogen attack (hydrogen forming metal hydrides with tanks materials).

A last point to consider is the source of hydrogen. Currently, most hydrogen is produced using the Steam Methane Reforming process (Kumar Agarwal and Valera, 2021; Osman et al., 2021). This process emits \mathcal{CO}_2 emissions and produces so-called gray hydrogen. For true emission-free hydrogen, electrolysis from renewable energy could be considered, also known as green hydrogen. A summary of section 2.2 is given in Table 2.3.

2.3. Section conclusion 7

Table 2.3: Advantages and disadvantages of hydrogen as a energy source. (summary of section 2.2)

Advantages	Disadvantages
No fuel-bound carbon	High cooling losses due to peak temperatures
High energy density by mass	High auto-ignition temperature
	Lower break mean effective pressures
	Bigger engine required
	Difficult storage
	NOx by high peak temperatures

2.3 Section conclusion

In conclusion, the use of ammonia and hydrogen as alternative fuels for internal combustion engines offers advantages and challenges. Ammonia provides a higher energy density than hydrogen and more favorable storage conditions, with the significant benefit of not producing direct \mathcal{CO}_2 emissions. However, it faces challenges such as high latent heat of vaporization and ignition temperature, necessitating additional modifications for efficient combustion. Hydrogen, while also free from carbon emissions and having a high gravimetric energy density, encounters difficulties related to high peak temperatures, demanding careful storage solutions, and producing NOx emissions because of high combustion temperatures. Both fuels demonstrate their potential as cleaner alternatives, but each requires technological advancements and strategic adaptations to optimize their use efficiently and safely.

Chapter 3

On voyage simulations

Voyage simulations are important for engine simulations by providing representations of real-world conditions under which the engine operates. These models can help predict fuel consumption, emissions, and engine performance in various scenarios. Using these models, simulations can reduce the need for physical testing. This section of the literature review will focus on this aspect and the second subquestion:

How are engine models used in time domain models for voyage simulations?

3.1 Ship simulation models

As part of a voyage simulation, the ship itself must be modeled. An example of this can be found in Sui (2021). In this research, Sui describes multiple ways to model the ship. In Chapter 7, Sui used the full 3D coordinate systems to model the maneuvering of the vessel. With this model, the vessel can perform different maneuvers. This way of modeling is too complex for this project as it does not concern the exact position of the ship but the position in the voyage.

The more practical application by Sui is described in Chapter 2. Here, Sui uses the models introduced in Woud and Stapersma (2002). This model uses ship speed to determine the resistance coefficient of the ship. The coefficient is corrected for different effects and calculated back to a resistance for the ship. The resistance is then matched with a propeller model based on open water diagrams as described by Woud and Stapersma (2002).

While this results in a basic propulsion method, a sea state can also be added as described in Sui et al. (2020). Here, Sui et al. mention how to include the sea state to create more resistance for the sailing ship compared to a calm sea. The equation for calculating the sea state can be seen in Equation 3.1. When multiple sea states occur during a voyage, a mean sea state can be calculated as shown in Equation 3.2.

$$SM = \frac{P_{E,\text{service}} - P_{E,\text{trial}}}{P_{E,\text{trial}}}$$
(3.1)

$$SM = \frac{P_{E,\text{service}} - P_{E,\text{trial}}}{P_{E,\text{trial}}}$$

$$S\bar{M} = \frac{\sum_{i} SM_{i} \cdot P_{E,i} \cdot \Delta t_{i}}{\sum_{i} P_{E,i} \cdot \Delta t_{i}}$$
(3.1)

3.2 **Engine model requirements**

The first highlighted implementation is done by Vrijdag et al. (2009). Vrijdag et al. aim to simulate a Multipurpose Frigate from the Royal Netherlands Navy. The authors approach to the engine model is to make use of lookup tables. As the propulsion plant has been analyzed before, these tables are available inside the navy and also contain some turbocharger dynamics. The engine model encompasses more than only the engine, as it also includes the fuel pumps, the gearbox, and the shafts. Although Vrijdag et al. calibrate the model, it only corrects the other elements and not the engine itself.

3.3. Section conclusion 9

Another study on propulsion were done by Sui et al. (2020). Sui et al. makes us of analytical function for engine torque in the form of the second-order Taylor expansion. The engine torque is a function of engine speed and fuel consumption, and the coefficients are fitted from engine test data. This method was first introduced by Shi (2013). According to Shi, this analytical method has some drawbacks. For example, this model does not contain any engine dynamics and is limited to the boundary conditions to which the engine is tuned.

Zincir (2022) approaches the question from a simpler angle. The author is more focused on studying the emissions of ammonia when produced from different sources. The Well-to-Wake emission analysis aims to study the production emissions and different ratios of ammonia and diesel. Therefore, Zincir assumes two constant ammonia energy fractions based on the studied literature. Zincir does not investigate further on the engine side of the simulation. However, the article also contains details on the journey of the ship, which can be useful for the rest project.

When working in the conceptual design space, a transfer function can be used (Bassam, 2017). The transfer function can be used to include the delay time for the engine reaction delay (Equation 3.3). In Equation 3.3 Q(s) is the engine torque, which with speed can be used to calculate engine power, while Y(s) is the Fuel rack setting. Another method used by the author is the mathematical model, shown in Equation 3.4. In Equation 3.4, $Q_{\rm mcr}$, $h_{p,\rm mcr}$, and $n_{\rm mcr}$ are the values of the engine torque, fuel flow rate, and rotational speed at the maximum continuous rating. It is important to note that this study is aimed at the simulation and integration of hydrogen fuel cells, using the engine only as a base case to compare costs of operation and construction.

$$Q_{\text{eng}}(s) = \frac{K_y e^{-\tau s}}{1 + \tau_c s} Y(s)$$
 (3.3)

$$\overline{Q} = 0.5 \overline{h}_p^{\frac{2}{3}} + 1.5 \overline{h}_p^{\frac{1}{3}} \overline{n} - \overline{n}^2, \overline{Q} = \frac{Q_{\text{eng}}}{Q_{\text{mcr}}}, \overline{h}_p = \frac{h_p}{h_{p,\text{mcr}}}, \overline{n} = \frac{n_{\text{eng}}}{n_{\text{mcr}}}$$
(3.4)

3.3 Section conclusion

When looking at the different studies performed on voyage simulations, the main conclusion is that for the purpose of a voyage simulation, the engine is very simply modeled. This ranges from a lookup table with engine performance data to fitting the engine to other parameters, such as speed and fuel mass.

Chapter 4

On Combustion Engine models

As seen in Section 3, more simple engine models are used for voyage simulations. This part will first look at a comparison of all the most common used engine models, where after the focus will shift to Seiliger cycle modeling. The section closes with a small part on friction and a conclusion. This section aims to answer the third sub-question:

How can different internal combustion engine models be used to model the use of conventional diesel fuel?

4.1 Varying models

There are different ways to model an internal combustion engine, ranging from very simple to very complex. The type of model used will depend on the project itself. When accuracy or understanding is important, a CFD simulation is likely to fit. If speed of the simulation matters most, a more simpler model like the thermodynamic cycle will be useful. The different types of models were identified by Alberer et al. (2011) and similar before by Rakopoulos and Giakoumis (2006). The authors list the following models. The summery of the advantages and disadvantages can be found in Table 4.1.

- 1. Mean value models (MVM). Mean value models do not take into account in-cycle variations, such as pressure or flow, but try to predict the mean value of the different variables. In addition, the system is broken down into a limited number of stages as described in Section 4.2. This type of model does not take the geometry of the engine into account and is therefore referred to as 0D models. Two different families of models can be differentiated inside this model. Data driven models (DDM) are derived from mathematical fitting engine data to models. The drawback is that the model is not based on physics and predicting capabilities can be limited. An advantage is that this type of model is very fast and can be even faster than the engine itself, allowing for optimization in predictive control. The other type is the mean-value engine model (MEVM). This type is based on the conservation equation such as the conservation of mass. The models can be very modular, allowing the swapping of different components used to model the entire engine. The 2 models can be combined into so-called gray box models, based on physics but tuned with data.
- 2. Emptying-and-filling models (E&FM). E&FM describe the in-cycle variations neglected by the mean-value models. This results in better insight into the process in the cylinder. The models again do not include the geometry, which classifies them as 0D models. The models are sometimes referred to as crank angle solved modes as the calculations are done as a function of crank angle instead of time, and thus present the in-cycle variation as a function of crank angle.
- 3. Wave action models (WAM). Wave action models include a 1D description of the intake and exhaust manifolds. The models includes the conservation of momentum allow for the simulation of a pressure wave. As pressure influences air flow at the intake and exhaust, the wave pressure peak will cause changes. WAM's intake descriptions are usually combined with E&FM.

4. Multi-dimensional models. Given a full geometric description of the cylinder, the Navier-Stokes equations can be formulated and solved. The CFD simulation solution answers complex questions such as 3D mixing. The disadvantage of CFD is the extremely high computational costs with the heavy calculations. Certain shortcuts such as RANS or LES can shorten the calculation time. To fully simulate the process in an internal combustion engine ignition models, chemistry models and more should be used, increasing computational costs even more.

As concluded in Section 3.3, only the more simple models are used in voyage simulation; therefore, the next part will focus on the Seiliger model in Section 4.2.

	DDM	MVEM	E&FM	WAM	CFD
Spatial resolution	0D	0D	0D	1D	3D
Physical description	no/very low	low	low	medium	complex
Prediction capabilities	no	low	medium	medium	high
Computational cost	very low	low	medium	high	very high

Table 4.1: Main characteristics of the different modeling techniques (Alberer et al., 2011).

4.2 Seiliger modeling

A possible way to describe the performance of an engine is the Seiliger process or cycle. This is a so-called 0-D process because it does not take the geometry of the engine into account. A description of this process can be found in Heywood (2018) and Stapersma (2010). Below, a short summary of the cycle will follow. The Seiliger cycle starts with isentropic or polytropic compression when the piston moves from the inlet valve closing to the TDC. The next phase is combustion and heat addition. After the compression follows an isochoric pressure rise. When the piston starts to move again, the heat input will continue with a part isobaric expansion. The cycle also includes an isothermal expansion part after which the combustion ends. The next part is an isentropic or polytropic expansion. When the exhaust ports are opened, the useful part of the expansion ends. The final part of the cycle is the expelling of the exhaust gases, which closes the cycle back to the start. A graphical representation can be found in Figure 4.1.

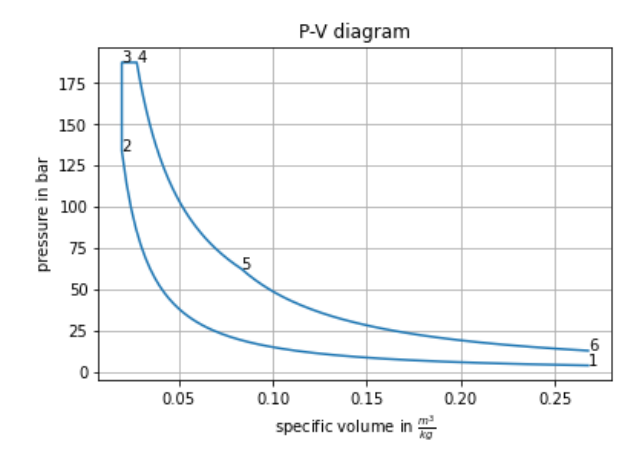


Figure 4.1: Example of a Seiliger cycle (based on the formulas in Stapersma (2010))

A possible way to improve the Seiliger model is shown in Murphy et al. (2015) and Ding et al. (2018). Where in the most basic approach it is to take c_v and c_p as constants, Murphy and Ding aim to improve the accuracy by changing this aspect. The heat capacities are assumed to be a power series of temperature. The coefficients for the power series are found in literature or found experimentally. These improvements have been tested on both engines, after which the authors conclude that for an accurate simulation, these effects cannot be neglected.

4.3. Friction modeling

The fitting of a six-point Seiliger model has been done in Sui et al. (2017). In this paper, Sui describes the process of fitting engine measurements to a six-point cycle. The process has been introduced in Ding et al. (2012), but this method aims only to model one point, while Sui fits to a wider engine envelope. This process can be described in 5 steps. The first step is to develop a heat release model from the measured pressure based on the ideal gas law. The second step is to fit a Vibe combustion model. This is followed by the in-cylinder process simulation model in step 3. The fourth step is to fit a Seiliger model, which is used in step 5 to determine the combustion parameters. Sui assumed the combustion parameters to be a function of the normalized engine speed and normalized fuel mass. The result is a combustion model that, in theory, is able to predict the parameters for a wide range of operating conditions. Research on the difference between the Seiliger cycle and Wiebe functions has been done by Sapra et al. (2020), which shows that the differences between the two approaches are small. Therefore, the Seiliger model approach will continue to be used.

4.3 Friction modeling

To get from the mean indicated pressure to the mean effective pressure, the mean friction pressure should be modeled. There are different ways to model the friction. The most widely used model is the Chen-Flynn model. The original model proposed by Chen and Flynn (1965) describes the friction pressure as a function of constant, the maximum cylinder pressure, and the engine speed (Equation 4.1). The constant takes into account the losses of the appendices. The maximum cylinder pressure is related to the load of the engine, because higher pressures lead to higher mechanical losses. The engine speed relates the increase in losses with an increase in speed.

$$FMEP = A + B \cdot P_{MAX} + C \cdot n + D \cdot n^2$$
(4.1)

This model has been further researched by Pipitone (2009). He proposes to make variations on this model by using higher powers on the max cylinder pressure. He finds a small improvement in correlation and continues by including spark ignition, leaving the scope of this project. A different way to correlate FMEP is presented by Finger (2021). Finger relates the friction to the current mean indicated pressure and a nominal mean indicated pressure. On the engine Finger tested this correlation, it yielded better results than the Chen-Flynn correlation. The note on these results is that the correlation is only tested on a diesel 4-stroke engine. Another point is the fact that according to the author 2 curves will exist: 1 for generating mode and 1 for propeller mode.

$$p_{m,f} = A \cdot e^{B \frac{p_{m,\text{ind}}}{p_{m,\text{ind},n}}} \tag{4.2}$$

When determining friction, an other approach can also be taken. The components of the engine could also be taken as different components, all contributing to friction. This is done, for example, by Livanos and Kyrtatos (2006). This method can be used to predict FMEP in a way comparable to the Chen-Flynn correlation.

4.4 Section conclusion

In conclusion, the section explored various internal combustion engine models used for simulating the use of conventional diesel. It highlighted the diversity of model complexities, from simpler, less computationally intensive mean value and emptying-and-filling models to more complex computational fluid dynamics models. Each type of model offers its own advantages, trade-offs in accuracy, and computational cost. In addition, more focus went to the Seiliger process as the selected method, with emphasis on possible improvements to the basic model. An additional point of attention was the friction modeling in engines, where different models exist to estimate losses.

Chapter 5

On dual-fuel engine models

As ammonia does not burn easily on its own and hydrogen is not very stable, one solution is to use a pilot fuel. This pilot fuel will start the combustion process, after which the second fuel will burn. The pilot fuel usually consists of diesel, as the conditions in an ICE are favorable for this fuel. This adds back CO_2 , but makes the use of cleaner fuels more feasible. This part of the literature review will first look at the models used for the dual-fuel engine in section 5.1. In section 5.2 & 5.3 will discuss the inclusion of the respective ammonia and hydrogen in the model. This part ends with a conclusion in Section 5.4 and an answer to the fourth question:

How can dual-fuel combustion be modeled with ammonia and hydrogen?

5.1 Model of Dual-fuel engine model

Modeling a Dual-Fuel engine requires changes to the standard model. A great example of the modification made is Van Duijn (2021). In his MSc thesis Van Duijn describes the process of incorporation of ammonia as fuel in the TU Delft engine B model. Here are the most important changes to the model.

The first is a change in the fuel supply. The ammonia energy share ratio is added, which controls which part of the energy is supplied by ammonia. This also changes the fuel rack from the fuel mass added to the energy added. The second change is in the description of the seiliger process. Although the stages themselves are not changed, the parameters a, b and c are. The assumption is made that the combusted fuel is of even parts ammonia and diesel, so when 40% of the available ammonia has burned, also 40% of diesel is burned. Van Duijn notes that for ammonia this is probably not correct as it has a slow flame velocity and more time is required to inject all the ammonia mass into the cylinder.

The third change is related to the Seiliger parameters. Here, the author includes both the pilot fuel and ammonia when calculating the a and b parameters. The ignition delay is the fourth, which only influences parameter a in the model. By using a correlation of the ammonia energy ratio with the ignition delay at full engine power, the author attempts to capture the new delay. The fifth change is in the air excess ratio, which now includes ammonia in the calculation because the air/fuel ration differs for ammonia. An aspect that has not changed is the combustion efficiency. While Van Duijn points towards Reiter and Kong (2010) to claim that the efficiency is maintained at the same level.

The last changes are made to the gas mixture and thermodynamic properties. The gas mixture is changed to include the stoichiometric exhaust gas of ammonia combustion. This also changes the thermodynamic properties as c_v and c_p . The method described above has been investigated with ammonia. Similar changes can be made to use hydrogen in the model. The next sections will focus more on the fuel combustion itself.

5.2. Ammonia

5.2 Ammonia

One of the first studies on the ammonia-diesel dual-fuel concept is conducted by Reiter and Kong (2010). Their experiments are performed using a 4-stroke high-speed engine. Reiter and Kong makes use of low-pressure injection, in which ammonia is mixed with fresh air intake and injected into the cylinder. Reiter and Kong tested the ammonia to diesel energy ratio mainly in a constant power mode. In this mode, the ammonia and diesel energy is mixed to obtain a set power. The results of the specific fuel consumption can be seen in Figure 5.1. The BSFC of a specific fuel is defined as its mass flow rate divided by the power output resulting from this specific fuel only, but not the overall power output of the engine. 2 different correlations can be seen in Figure 5.1: Firstly, with a lower contribution of diesel, the diesel sfc increases. Reiter and Kong think the conditions are similar to light-load operation, resulting in lower efficiency (Heywood, 2018). The ammonia sfc is the best at this point, which is not explained by the authors. Secondly, with the high-energy contribution of diesel, the effects are reversed. The authors explain this effect as the result of the mixture becoming too lean to have good flame propagation. Given these results, Reiter and Kong would aim to keep the ammonia energy ratio between 40% and 60% to keep a good fuel efficiency.

The second point in this paper is the combustion temperature when ammonia is added. As the diesel percentage increases, the peak pressure and temperature decrease. The peak pressure is also delayed in time as the ammonia is harder to ignite because of the higher auto-ignition temperature. The effect of lower cycle temperature can also be seen in the measured exhaust. As the ammonia part increases, this leads to lower temperatures and therefore to worse combustion of the diesel and to more CO and incomplete combustion product emissions. As a final note on this paper regarding the project, the engine tested is a high-speed 4-stroke engine, therefore the results might not fully apply to a slow-speed 2-stroke marine engine.

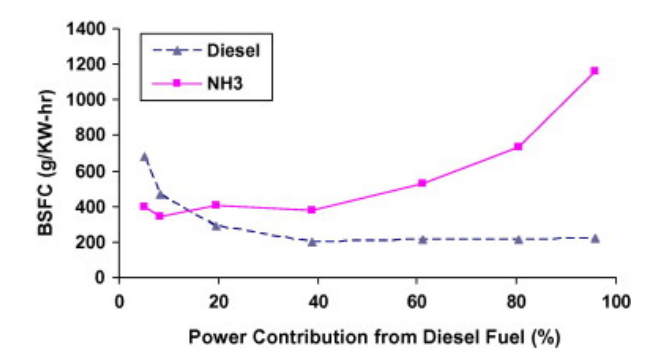


Figure 5.1: Measured engine BSFC data for respective fuels under constant power output operation using various combinations of ammonia/diesel fuel. (Reiter & Kong, 2010)

While Reiter and Kong investigated the larger range of energy share and concluded that equal parts of ammonia and fuel should be used, other research has been carried out in higher percentages of ammonia. An experimental recent study has been performed on a 4-stroke medium-speed engine with direct injection in Park et al. (2024). In this study, Park et al. aim to decrease pilot fuel consumption in order to reduce GHG emissions. However, Park et al. (2024) find that the decrease in pilot diesel fuel leads to a decrease in combustion efficiency and a significant increase in unburned ammonia. Park et al. also notes that low load conditions decrease combustion stability. This is experienced by Reiter and Kong (2010) when testing their second testing setup. To optimize the efficiency of the test engine, Park et al. tested with different diesel injection timing. They found that an optimal injection time could be found and that the timing stayed constant for a constant energy ratio, even under part load conditions. Similar results are produced in Yousefi et al. (2021) in simulations.

5.2. Ammonia

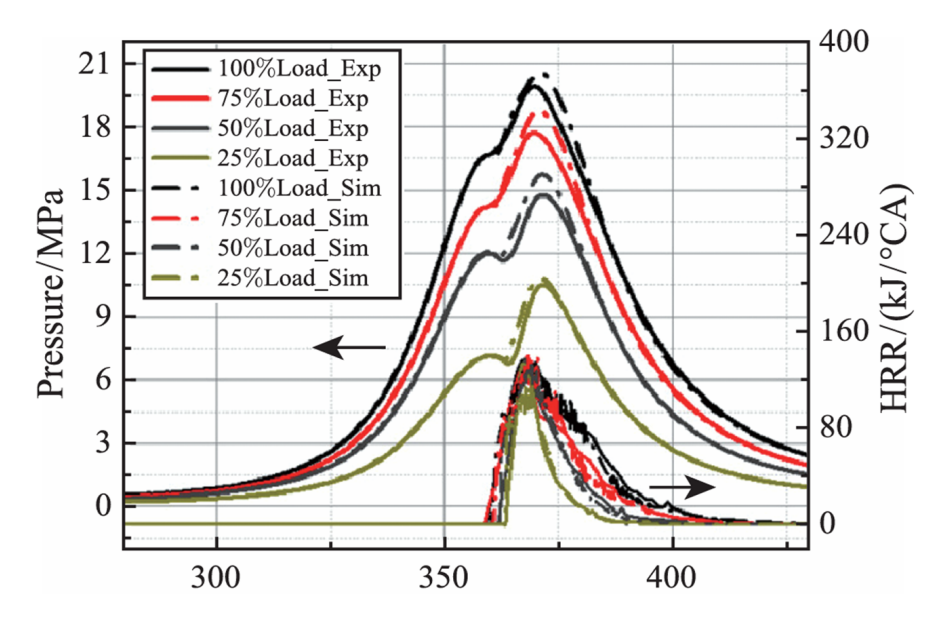


Figure 5.2: Heat release rate of ammonia-diesel combustion at constant ammonia energy ratio at varying loads. (Cui & Wang, 2023)

When it comes to large 2-stroke slow-speed engines, few experimental studies have been conducted. The results of an experimental study can be seen in Cui and Wang (2023) and Figure 5.2. In this paper, Cui and Wang created a CFD model for injector strategies for diesel-ammonia engines. The ammonia energy percentage used in this engine was 95%. This data can be used as a basis for the engine modeling. The related data can be found in Table 5.1. Wu et al. (2024) continues on this paper with a CFD model that looks at different variables to improve performance. These variables are the injection pressure, ammonia injection timing, and a split ammonia injection.

Table 5.1: Engine data used by Cui and Wang (2023)

Parameter	100% Load	75% Load	50% Load	25% Load
Speed / rpm	103.0	94.0	82.2	65.3
Explosion Pressure / MPa	19.93	17.73	14.75	10.5
Indicated Power / kW	9670	7355	4974	2580
Effective Power / kW	9010	6813	4560	2312

Another informative study on the diesel-ammonia engine can be found in X. Zhou et al. (2022). X. Zhou et al. use CFD simulations to study different aspects of low-pressure injection and high-pressure direct injection. Although the low-pressure injection is less relevant to this project, the high-pressure injection is rather relevant. X. Zhou et al. show at first the heat balance of the engine for different diesel energy ratios. This figure can be found in Figure 5.3. From this graph, it can be seen that the increase in the diesel energy ratio seems to lead to an increase in combustion efficiency. X. Zhou et al. claims this effect happens because that the larger volume of ignition source at the higher energy fraction favors sufficient combustion of the following injected liquid ammonia. The last study to be discussed is done by Zhang et al. (2022). In this study, Zhang et al. investigate the feasibility of liquid ammonia/diesel direct injection. This is done by varying the ammonia injection duration and therefore injection amount while keeping diesel injection constant. The results are studied at the maximum engine speed of 375 rpm. The pressure and heat release rate show that, for higher ammonia amounts, the pressure and HRR peaks occur later. The ammonia energy ratio in this experiment is between 40 and 50 %.

5.3. Hydrogen 16

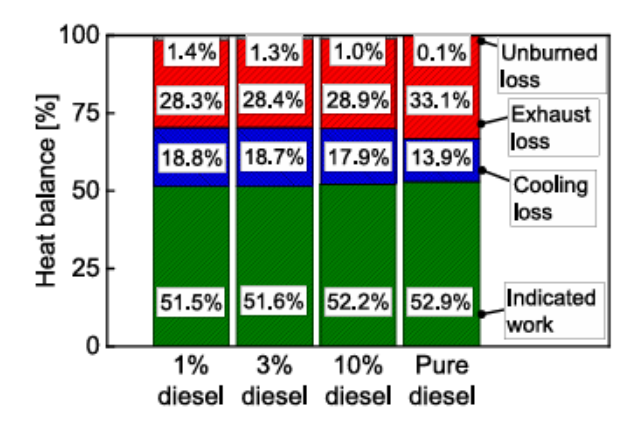


Figure 5.3: Heat balance under different diesel energy fraction for the HPDF mode. (X. Zhou et al., 2022)

5.3 Hydrogen

One complication with Hydrogen as a fuel, is the high auto-ignition temperature (Table 2.1). However, the activation energy of hydrogen is low and it requires little energy to ignite. This can be done with a spark plug (Seddiek et al., 2015) or with the use of a pilot fuel (Serrano et al., 2021). One of the first studies on the application of hydrogen is done by El-Gohary (2009). In this study, the author describes a proposal for a 4-stroke hydrogen engine. The cycle assumed to calculate the efficiency is the otto cycle. This is based on the high combustion rate of hydrogen. This concept is further investigated in Seddiek et al. (2015). Here, Seddiek et al. also include a 2-stroke direct injection engine. The 2stroke concept is seen as the better alternative, because higher compression ratios can be reached with the risk of explosions because fuel is only injected after compression. They however also find that this engine has a rather low efficiency when compared to the diesel engine (30% vs. 47%). In their case study, this results in a much shorter operational time of the vessel as not enough fuel storage is available. Another point to note is the high temperature reached when burning hydrogen. As there is rapid combustion at top dead center, there will be increased temperatures and thermal generated NOx emissions (Zincir et al., 2023). A possible way to counteract this is through exhaust gas recycling (EGR) (Wang et al., 2018). EGR increases specific heat and reduces oxygen concentration, resulting in a lower peak temperature and NOx formation.

An alternative to a pure hydrogen engine is a hydrogen-diesel engine. The hydrogen ignition is then caused by the injected diesel fuel. This adds back in CO2 emissions, but does not require a spark plug or high internal ignition temperature. An application of the dual-fuel hydrogen concept is done by Serrano et al. (2021). In this study, Serrano et al. investigate the low pressure injection of hydrogen with water in a marine engine. The water is added to prevent unwanted self-ignition and combustion knocking as well as to reduce the NOx emissions of the engine. The water injection as previously tested on 4-stroke engines with only hydrogen (Serrano et al., 2019b) and dual-fuel hydrogen (Serrano et al., 2019a).

5.4. Section conclusion 17

5.4 Section conclusion

In conclusion, there are several important remarks to model the use of ammonia and hydrogen in dualfuel engines. From Van Duijn (2021) it can be concluded that it is important to change the parameters involved to include alternative fuels. The most relevant are the Seiliger parameters a, b, and c, but also the thermodynamic constants and fuel-related variables.

Research into high-pressure direct-injection diesel engines for both dual-fuel ammonia and hydrogen is scarce. One study involving experimental data on ammonia is Cui and Wang (2023), which allows for a basis for modeling the cycle. Another important study is X. Zhou et al. (2022). Based on simulation data, X. Zhou et al. show the energy balance for different ammonia energy percentages, which is helpful to model the engine. Studies on hydrogen high-pressure direct-injection are more scarce. Hydrogen as a fuel will probably behave as a high-reactive fuel, resulting in a lower-efficiency engine. Several methods can be applied to increase engine efficiency, such as EGR and water injection.

Research

Chapter 6

Voyage simulator

This chapter will discuss the creation of the voyage simulator model. The model will include all parts for running simulations on the Duisburg vessel. The mathematical model of the vessel is based on the test data available for the Duisburg Test Case (Moctar et al., 2012). The model can be broken down into three important sections. The first is the resistance of the ship in water in section 6.1. The second is the propeller with the open-water diagram in section 6.2. The third model is the engine model which will be described in more detail in section 6.5.

The mathematical model is implemented in MATLAB Simulink (Figure 6.1). The model can be divided into six main components that communicate with each other via variables. The orange block contains the engine models. This block takes the speed of the engine n_e and computes the engine torque M_e for the propeller. The green block on the right is the resistance model, which calculates the total resistance R_T from the current speed of the vessel v_s . The blue block in the middle is the propeller model that uses the propeller advance velocity v_a and the rotational speed n_p to calculate the propeller thrust T and torque Q. The 2 yellow blocks contain the connections between the main code blocks. For simulation control, the light blue control block is provided, which contains the code for the fuel rack position for the engine. The separate blocks are described in more detail in the following sections.

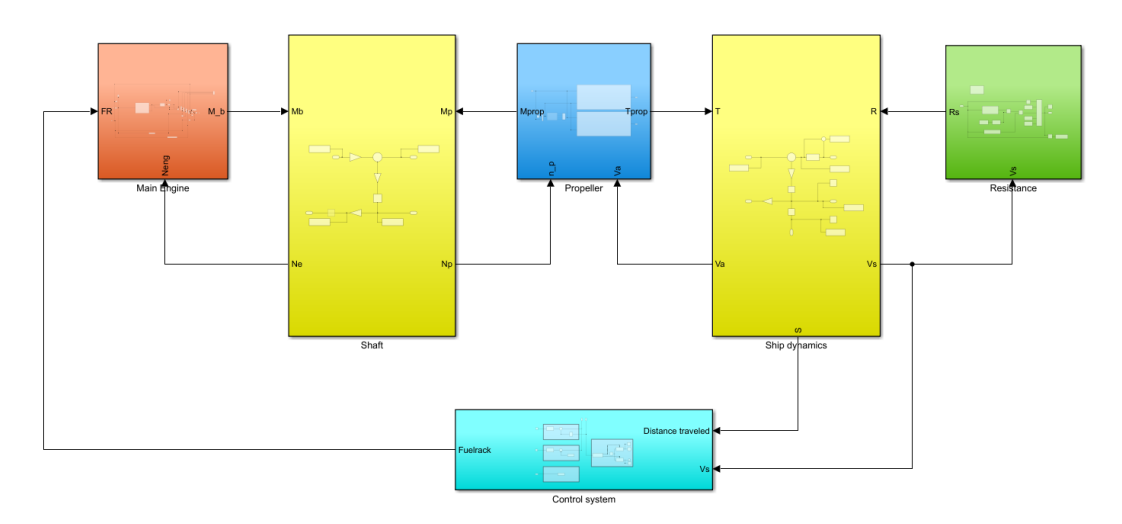


Figure 6.1: Simulink model layout

6.1. Resistance 20

6.1 Resistance

The Duisburg container vessel was tested for a speed of 20.0 to 25.0 knots. The model test data can be seen in Table 6.1. From these test data of the model, several non-dimensional resistance coefficients were calculated. The total resistance coefficient is found using the model resistance and Equation 6.1. In this formula R_T is the measured resistance of the model, ρ the density of the testing medium, S_w the wet area of the model hull and v the speed of the vessel. The friction coefficient \mathcal{C}_f is calculated using the ITTC 1957 using the Reynolds number as shown in Equation 6.2. The wave resistance coefficient is calculated using Equation 6.3 with k being the form factor. The form factor was found from RANS-CFD simulations as k = 0.094 for the model scale and k = 0.145 for full scale.

v_S [m/s]	v_M [m/s]	Fr [-]	$Re \cdot 10^6$ [-]	R_T [N]	R_F [N]	$C_T \cdot 10^3$ [-]	$C_F \cdot 10^3$ [-]	$C_W \cdot 10^4 \text{ [-]}$
20.0	1.335	0.174	7.319	20.34	17.611	3.661	3.170	1.932
21.0	1.401	0.183	7.681	22.06	19.229	3.605	3.142	1.672
22.0	1.469	0.192	8.054	24.14	20.964	3.588	3.116	1.791
23.0	1.535	0.200	8.415	26.46	22.713	3.602	3.092	2.194
24.0	1.602	0.209	8.783	28.99	24.554	3.623	3.069	2.660
25.0	1.668	0.218	9.145	31.83	26.431	3.670	3.047	3.360

Table 6.1: Resistance data from the Duisburg model tests

$$C_T = \frac{R_T}{0.5\rho S_w v^2} \tag{6.1}$$

$$C_T = \frac{R_T}{0.5\rho S_w v^2}$$

$$C_f = \frac{0.075}{(\log_{10} Re - 2.0)^2}$$
(6.1)

$$C_w = C_T - (1+k)C_f (6.3)$$

$$R_T = 0.5 \cdot C_T \rho S_w v^2 \tag{6.4}$$

Given these data, certain parts of the simulation data can now be calculated. The wave resistance data is visualized in Figure 6.2. In these data a quadratic trend line is added. The trend line fits properly in the area with the available data. However, at slower speed, the data is missing, resulting in a poorer fit. This even allows the coefficient to become negative, which is unrealistic. It must be considered that the coefficient is much smaller the friction coefficient in the known data and even smaller at the negative part. In addition, the ship is not expected to sail at these low speeds; therefore, it is reasonable to accept this trend for further processing.

Again using the ITTC formula from Equation 6.2, the friction component is calculated using the Reynolds number of the full-scale vessel. This coefficient is corrected for the form factor and added to the wave resistance. Using Equation 6.4, the full-scale resistance can be calculated for each speed. The effective towing power P_e is also calculated using $P_e = R_T \cdot v$. Figure A.2 shows the implementation of the resistance model in the Simulink simulation.

6.2. Propeller 21

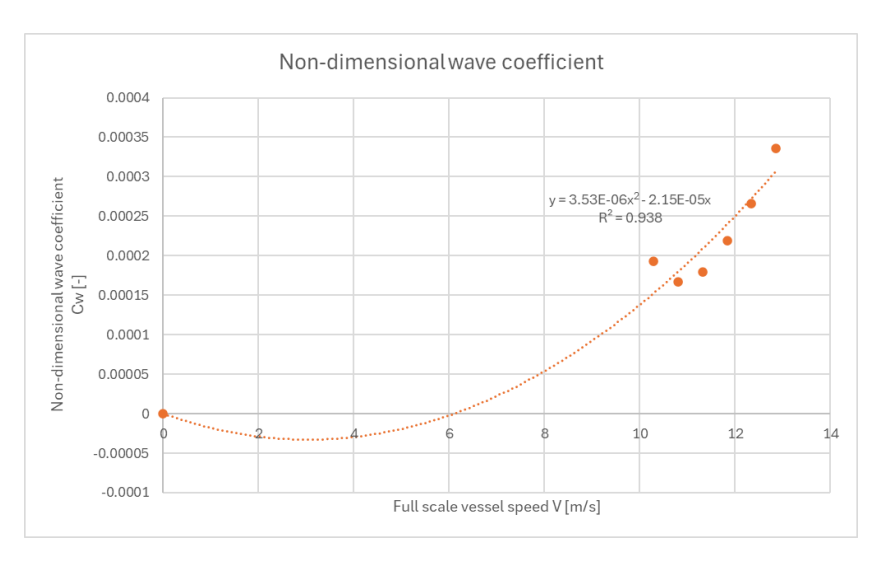


Figure 6.2: Wave resistance coefficient as a function of the full scale vessel with trend line

6.2 Propeller

The Duisburg propellor has also been tested in open-water tests. In the open-water test measured Thrust T and Torque Q are turned into non-dimensional thrust (K_T) and torque (K_Q) coefficients using Equations 6.5 and 6.6. The open-water efficiency η_o is calculated using Equation 6.7. The advance ratio J is determined using Equation 6.8. In the next equations, the following variables are used: D_P [m] is the diameter of the propeller, n [hz] is the rotation frequency of the propeller, ρ [kg/m³] the density of water, ω [rad/s] the angular propeller speed and v_a [m/s] the advance velocity of water at the propeller.

$$K_T = \frac{T}{\rho D_P^4 n^2} \tag{6.5}$$

$$K_Q = \frac{Q}{\rho D_P^5 n^2} \tag{6.6}$$

$$\eta_o = \frac{P_T}{P_D} = \frac{T \cdot v_a}{Q \cdot \omega} \tag{6.7}$$

$$J = \frac{v_a}{nD_P} \tag{6.8}$$

The results are shown and visualized in Figure 6.3. A quadratic fit works well for the open-water diagram. R^2 is a measurement of the quality of the fit. For both fits R^2 is high, indicating an almost perfect fit to the data. Table 6.2 shows the coefficients to be filled in Equation 6.9. The Simulink results are shown in Figure A.3.

$$K_{T/O} = A \cdot J^2 + B \cdot J + C \tag{6.9}$$

Table 6.2: Correlation coefficients for a quadratic trend line

	Α	В	С	R^2
K_T	-0.0975	-0.419	0.0513	0.9998
K_Q	-0.016	-0.0485	0.0715	0.9999

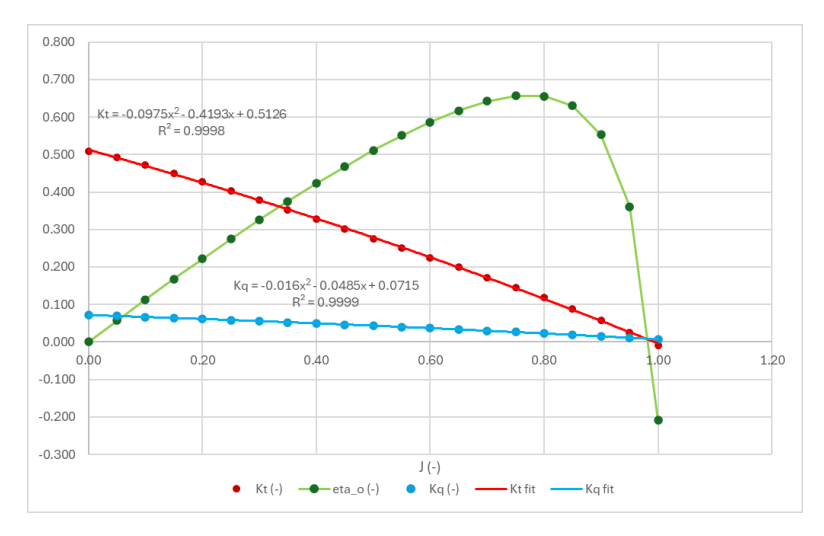


Figure 6.3: Openwater diagram from the available data from the Duisburg Test Case

6.3 Wake fraction and Thrust deduction

The last part of the mathematical "wet" model is the propulsion tests. Using data from other tests, the thrust deduction factor t, the wake fraction w, and the hull efficiency η_h are calculated for implementation. These values vary a small amount with speed but show no clear trend. With a small part of the available range of speed, nothing is known about lower speeds. However, with resistance, it can be trusted that the larger viscous resistance dominates the overall resistance. The viscous resistance is also given by ITTC 1957 in relation to the ship speed. In contrast, there is no basis for the thrust deduction and wake fraction. Therefore, while less correct, these values are taken as constants in the model, resulting in mean t=0.0925 and w=0.276.

v [m/s]	t [-]	w [-]	η_h [-]
10.29	0.081	0.264	1.249
10.8	0.101	0.279	1.247
11.32	0.093	0.277	1.255
11.83	0.089	0.281	1.266
12.35	0.101	0.277	1.245
12.86	0.090	0.275	1.255

Table 6.3: Thrust deduction factor, wake fraction and hull efficiency

6.4 Ship and Shaft dynamics implementation

To convert forces and torques to ship speed and propeller speed, the dynamics blocks are used. The Ship dynamics block, shown in Figure A.4, compares the produced thrust at the propeller with the ship resistance as calculated in the resistance block. The thrust deduction is added to the resistance. When the resulting force is divided by the mass of the vessel, it provides the acceleration of the vessel. The acceleration is integrated to evaluate the ship speed v_s . The speed of the ship is used for the resistance calculation and for the advance velocity v_a with the wake fraction. The advance velocity is fed back to the propeller. Finally, the speed of the ship is integrated again to obtain the distance traveled, which can be used for the control system.

The shaft dynamics are handled similar to the ship dynamics. Figure A.5 shows the shaft implementation. The torque provided by the engine M_b is compared to the torque requested by the propeller M_p . The resulting torque is divided by the inertia of the shaft. The shaft inertia also includes the inertia of the entire propulsion system of the engine and propeller. The shaft acceleration is integrated to obtain

the shaft speed and the propeller speed n_p . The model includes the possibility of using a transmission to alter the engine speed n_e with respect to the propeller speed. However, the Duisburg will be using a 2-stroke low-speed engine, which makes the transmission unnecessary, and therefore the gearbox ratio is set to 1.

6.5 Internal Combustion Engine

The engine model must compute the output torque of the engine given the input fuel mass of the fuel rack. The model is broken down in the following pieces: First, the fuel specific heat input q_f is transformed into Indicated specific heat input q_i . Then, the Seilinger cycle will be used to compute the indicated specific work w_i . The Seiliger cycle uses a set of processes to calculate pressures, volumes, and temperatures. The 5-point cycle consists of 4 stages:

- 1. (1-2) Isentropic or polytropic compression
- 2. (2-3) Isochoric combustion (or heat addition at constant volume)
- 3. (3-4) Isobaric combustion (or heat addition at constant pressure)
- 4. (4-5) Isentropic of polytropic expansion

The governing formulas for the Seiliger cycle can be derived from Stapersma (2010) and Heywood (2018). Finally, mechanical losses must be taken into account to calculate output work and torque. The turbo charger must also be modeled to compute the starting pressure.

General engine

This subsection will explain the first high-level model of the engine and is shown in Figure A.7. This figure shows the input on the left and the output on the right. The fuel rack FR is an input from the control system and is the fraction of the nominal fuel flow to the engine. The minimum and maximum are checked with a saturation block. This prevents the engine from running too fast or too slow or keeping the engine power below maximum power. The fuel rack is converted to a diesel fuel mass per cycle and is inputted further into the model. The engine block is shown below in Figure A.8 and contains the Seiliger implementation. On top is the engine block, the exhaust system with the turbo charger to calculate the starting pressure. The output of the engine block is the engine torque for the propeller.

The next step in the engine is the Seiliger application in Figure A.8. The input pressure from the turbo charger is used for the start of the entire Seiliger simulation process and for the calculation of the trapped air mass. The Seiliger process is divided into separate steps as outlined earlier and is represented as orange blocks. The light blue block embodies the heat release of the fuel into the cylinder and dictates the amount of specific energy for the different combustion processes. The two green blocks are for data collection and are communication using the to/from block in Simulink (removed in these images for clarity). This part of the model contains the mechanical losses that are a function of the engine speed. The available heat in the exhaust is in the top right corner. The specific work of each process is added and multiplied with the air mass to get the indicated work. The mechanical losses are subtracted and the effective work is transformed into the torque output of the engine. The next subsections will define the formulas used in the different parts of the model.

Heat input

The fuel specific heat input comes from the heat contained in the injected fuel. The extractable heat is the product of the injected fuel mass m_f and the lower heating value of the fuel or the fuel mixture h_L (Equation 6.10). Some of this fuel does not combust, which will keep the energy in the fuel to be ejected out with the exhaust gasses. The heat added with the combusted fuel q_{comb} is q_f minus the energy of the fuel that is not combusted. The combustion efficiency η_{comb} is defined in Equation 6.12. The combustion efficiency depends on different variables. The combustion efficiency is generally very

high for diesel, producing very low losses. The next step is the cooling losses because a part of the released energy is removed from the cylinder without contributing to the cycle. Heat losses are, among others, caused by conduction through the wall and head of the cylinder and the piston. These losses can also include the effects of the polytropic processes in the Seiliger cycle. By including the losses of the polytropic processes in here, the processes can be seen as isentropic. The conduction losses are proportional to the temperature difference between the inside and outside of the cylinder ΔT and can be assumed to be a function of engine load. The engine load relates to the peak temperature in the engine. Therefore, the fuel rack can be used to estimate the varying part cooling losses on top of the constant cooling losses. The heat input for the Seiliger process is described in Equation 6.13. The final part before the actual cycle is the heat division. Part of the heat will be inputted into the cycle at constant volume q_{cv} and the rest at constant pressure q_{cp} . These values should not be misinterpreted as heat capacities at constant volume and pressure (C_p and C_v). The division parameter X in a dieselusing engine depends on the engine speed. At lower speeds more heat is added at constant volume. As will be shown in chapter 8, the heat division parameter is influenced by alternative fuels. The use of the heat division parameter X is shown in Equation 6.14 and 6.15. The part of the model is shown in Figure A.9.

$$q_f = m_f \cdot h_L \tag{6.10}$$

$$q_{comb} = q_f - q_{comb,loss} (6.11)$$

$$q_{comb} = q_f \cdot \eta_{comb} \tag{6.12}$$

$$q_i = q_{comb} - q_{cool,loss} (6.13)$$

$$q_{cv} = q_i \cdot X \tag{6.14}$$

$$q_{cp} = q_i \cdot (1 - X) \tag{6.15}$$

Stage 1-2: Isentropic compression

The first step in the actual cycle is compression after closing the intake ports. The trapped air is compressed as the piston moves the top dead center. The process is assumed to be isentropic. This means that no heat is lost during the compression and the specific heat ratio γ_a is used instead of the polytropic compression factor N_c . The compression ratio R_c is the ratio between the compressed volume and the starting volume. T_1 , p_1 and v_1 are the starting values after the process begins. During this process, the system does negative work, as it requires energy to compress the air. Figure A.10 shows the first process of the Seiliger cycle.

$$T_2 = T_1 \cdot (R_c)^{\gamma_a - 1} \tag{6.16}$$

$$p_2 = p_1 \cdot (R_c)^{\gamma_a} \tag{6.17}$$

$$v_2 = \frac{v_1}{R_c} {(6.18)}$$

$$w_{12} = -\frac{R_a}{\gamma_a - 1} \cdot (T_2 - T_1) \tag{6.19}$$

Stage 2-3: Isochoric combustion

The second process is the heat addition at constant volume. During this process, the fuel starts to combust and adds heat to the process. A part of the fuel combusts almost instantly, resulting in a very fast increase in pressure, while no significant change occurs in crank angle and volume. The Seiliger parameter a is related to the heat input during this process and is used to calculate the next pressure and temperature. As no change in volume occurs, the system does not do any work. The isochoric combustion is shown in Simulink in Figure A.11.

$$a = \frac{q_{cv}}{C_v \cdot T_2} + 1 \tag{6.20}$$

$$v_3 = v_2$$
 (6.21)

$$T_3 = T_2 \cdot a \tag{6.22}$$

$$p_3 = p_2 \cdot a \tag{6.23}$$

$$w_{23} = 0 (6.24)$$

Stage 3-4: Isobaric combustion

The third stage is combustion under constant pressure. The piston starts to move back to the bottom dead center, and the volume increases again. Without heat input, this would result in a drop in pressure, as the process would become an isentropic expansion. With the combusting fuel, this results in a constant pressure during this process. The related Seiliger parameter is b is calculated with the heat input and the next temperature and pressure can be determined using this parameter. The work of the system is positive and adds to the work output of the cylinder. Figure A.12 shows the isobaric combustion.

$$b = \frac{q_{cp}}{C_p \cdot T_3} + 1 \tag{6.25}$$

$$p_4 = p_3 (6.26)$$

$$T_4 = T_3 \cdot b \tag{6.27}$$

$$v_4 = v_3 \cdot b \tag{6.28}$$

$$w_{34} = R_a \cdot (T_4 - T_3) \tag{6.29}$$

Stage 4-5: Isentropic expansion

The last stage of the 5-point Seiliger cycle is the isentropic expansion. This process is again assumed to be isentropic, so γ_a is used instead of the polytropic expansion coefficient N_e . The piston moves back to the bottom dead center. The ending volume v_5 is assumed to be the same as the starting volume v_1 . When the exhaust opens, the final heat is expelled from the cylinder with the exhaust gasses. The last process is shown in Figure A.13.

$$p_5 = p_4 \cdot (R_e)^{\gamma_a - 1} \tag{6.30}$$

$$T_5 = T_4 \cdot (R_e)^{\gamma_a} \tag{6.31}$$

$$v_5 = v_1 = \frac{v_4}{R_e} \tag{6.32}$$

$$w_{45} = -\frac{R_a}{\gamma_1 - 1} \cdot (T_5 - T_4) \tag{6.33}$$

Work output

After the cycle, a net result of the engine work is calculated. Only stage 12, 34, and 45 contribute to indicated specific work w_i Equation 6.34. The difference between engine output specific work w_e and w_i is mechanical loss. Mechanical losses $W_{m,loss}$ can be modeled as a constant part and a part as a function of the engine speed (section 4.3). The constant part of the mechanical losses comes from the auxiliary equipment. The second part scales with the engine speed as more friction occurs at high speed. The break torque M_b can be calculated using Equation 6.36. The break torque will be passed on to the propeller block of the model. For reference, the engine break power is calculated with Equation 6.37.

$$w_i = w_{23} + w_{34} + w_{45} \tag{6.34}$$

$$W_{m,loss} = W_{m,n} \cdot \frac{n_e}{n_{e,nom}} + W_{m,c}$$
 (6.35)

$$M_b = \frac{w_e \cdot m_a \cdot i_{eng}}{k_{eng} \cdot 2\pi} \tag{6.36}$$

$$P_h = M_h \cdot 2\pi \cdot n_e \tag{6.37}$$

The starting pressure p_1 can be derived using the turbocharger. The model for the turbocharger is from the Diesel Engine A model of the TU Delft and was first published in Miedema and Lu (2002) where the authors simplify the entire turbine and compressor in one equation. The available heat flow \dot{Q}_{51} in the turbocharger can be calculated using Equation 6.38. The pressure estimation is displayed in Equation 6.39. To build in a time delay on the turbo, the pressure is compared to the current pressure and then divided by τ_{TC} . The result is integrated with time as in Equation 6.40. The resulting pressure p_1 is fed back to the engine to restart the cycle.

$$\dot{Q}_{51} = \frac{C_v \cdot n_e \cdot m_a}{k_{eng}} \cdot (T_5 - T_1) \tag{6.38}$$

$$p_{1,est} = p_{amb} \cdot (\frac{c_{tc} \cdot Q_{51}}{C_p \cdot T_{amb}} + 1)^{\frac{\gamma_a}{\gamma_{a-1}}}$$
(6.39)

$$p_1 = \int \frac{p_1 - p_{1,est}}{\tau_{TC}} \cdot dt \tag{6.40}$$

Engine performance

To assess the efficiencies of the engine, several efficiencies are defined. The efficiencies of combustion η_{comb} and heat input η_q are related to the fuel input, whether it is diesel or a mixture. The thermodynamic efficiency η_{td} is related to the Seiliger cycle. However, the heat input at the different processes is related to the fuel. The mechanical efficiency η_m will be set at the nominal engine point and scaled with the engine speed, as explained earlier. Figure 6.4 shows the different types of heat and works as well as the losses.

$$\eta_{comb} = \frac{q_{comb}}{q_f} = \frac{Q_{comb}}{Q_f} \tag{6.41}$$

$$\eta_q = \frac{q_i}{q_{comb}} = \frac{Q_i}{Q_{comb}} \tag{6.42}$$

$$\eta_{td} = \frac{w_i}{q_i} = \frac{W_i}{Q_i} \tag{6.43}$$

$$\eta_m = \frac{w_e}{w_i} = \frac{W_e}{W_i} \tag{6.44}$$

$$\eta_e = \frac{w_e}{q_f} = \frac{W_e}{Q_f} = \eta_{comb} \cdot \eta_q \cdot \eta_{td} \cdot \eta_m \tag{6.45}$$

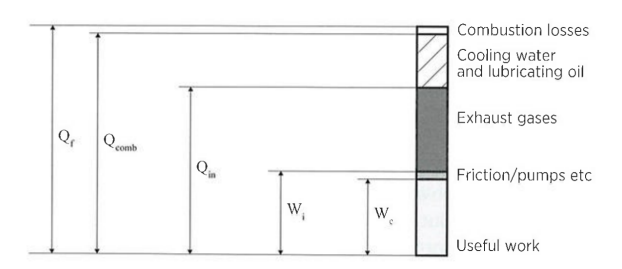


Figure 6.4: Visualization of the energy losses in an ICE (Woud & Stapersma, 2002)

6.6 Control systems

The last part of this section is the simulation control system. As can be seen in Figure 6.5, their are four options to govern the simulation. The first is the most simple solution, which can be seen in the lower left. In this case, the Simulink imports the fuel rack position as a function of time from the MATLAB workspace. The second system is the speed-time reference mode. In this mode, the current speed of the vessel is compared to an imported speed. A PID controller controls the fuel rack based on this signal. This mode allows for example one to change the speed of the vessel after a certain time without relying on the fuel rack position. This function can be seen on the middle left. The third option is the speed-distance mode. In this mode, the currently traveled distance is used in a lookup table to get the desired speed reference. The speed reference is then used as in the second mode to control the fuel rack via PID. The second and third modes are more computationally intensive, resulting in a longer simulation duration. The last mode is related to a stopping condition which allows for the simulation to be cut off after a certain distance traveled.

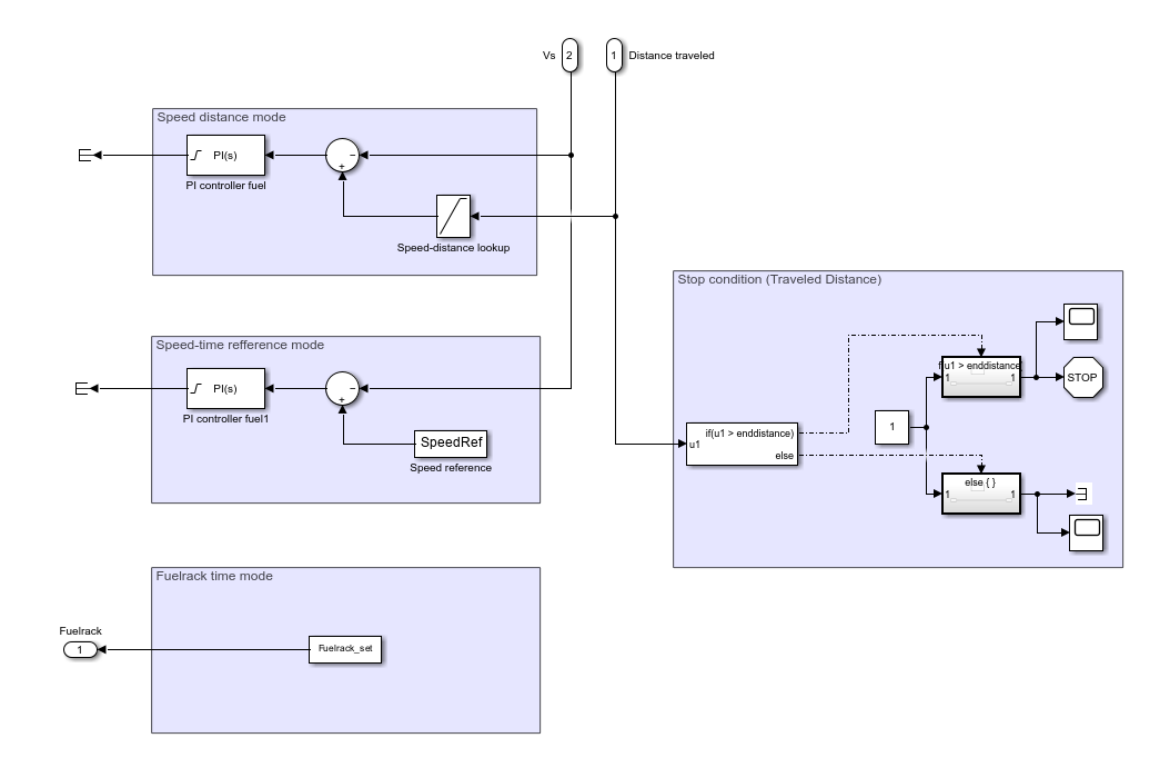


Figure 6.5: Simulink control system

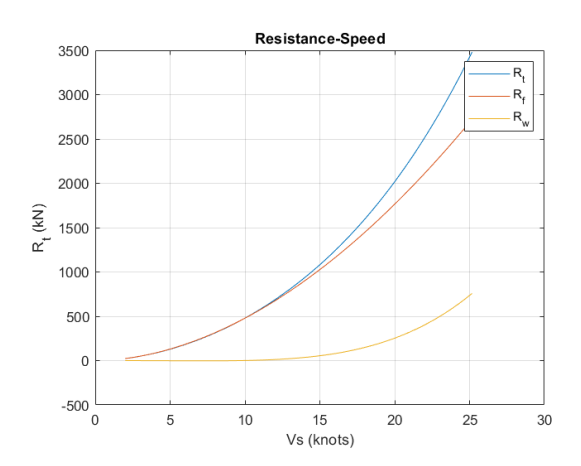
Chapter 7

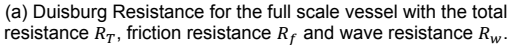
Intermediate results

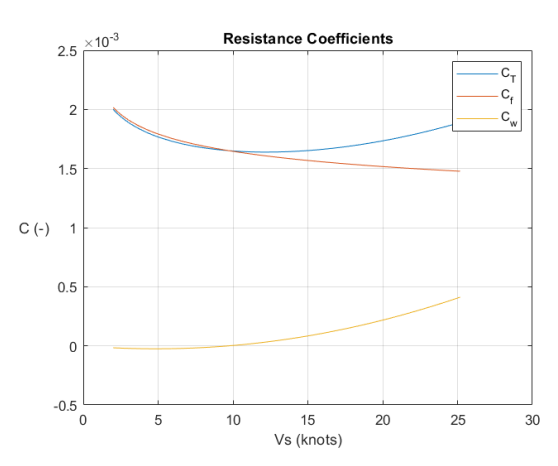
7.1 Model results

With the simulator complete, the resistance and propeller results can be analyzed. First, the total resistance of the vessel is shown in Figure 7.1a. The total resistance is broken down into wave resistance and friction resistance. From this figure it can be observed that, at lower speeds, the frictional resistance is almost the entire resistance. At higher speeds, between 15 and 25 knots, wave resistance is becoming a more significant part of the vessel resistance.

The resistance can be broken down into the different coefficients as explained in section 6.1. The results are shown in Figure 7.1b. This again shows that the wave resistance is very small at low speed, and the friction resistance dominates the total resistance. This figure also shows that the frictional resistance coefficient decreases with higher speeds, while the wave resistance coefficient increases. As these higher speeds are tested for the Duisburg in towing tests, this data can be regarded as very reliable, while the slower speed data is based upon the idea that the wave resistance goes to zero for low speeds.



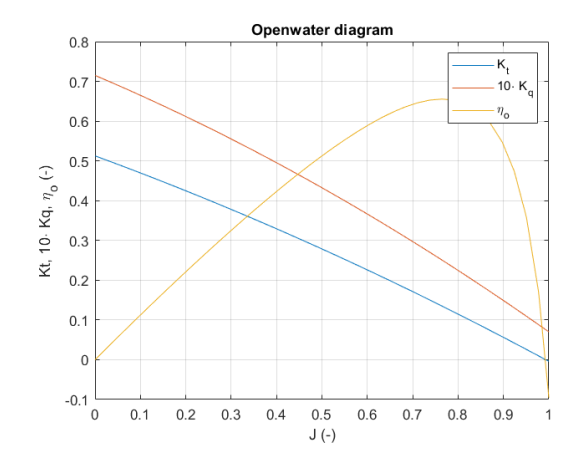




(b) Resistance coefficients for the total resistance \mathcal{C}_T , friction resistance \mathcal{C}_f and wave resistance \mathcal{C}_w

Figure 7.1: Resistance results from Simulink

The last part of this section is the open-water diagram. The values are almost identical to the open-water diagram shown in Figure 6.3 from the Duisburg paper. Any differences can be attributed to rounding errors in the correlation coefficients. Figure 7.3 shows the results of the turbo model with a turbo constant c_{tc} of 0.06. The available turbo power is based on the end temperature of the cycle. The figure shows the absolute pressure after the compressor. This figure also shows the weakness of this turbo model as without limits the pressures can rise unlimited. To keep the results realistic, the compressor pressure was capped at max 5 bar.



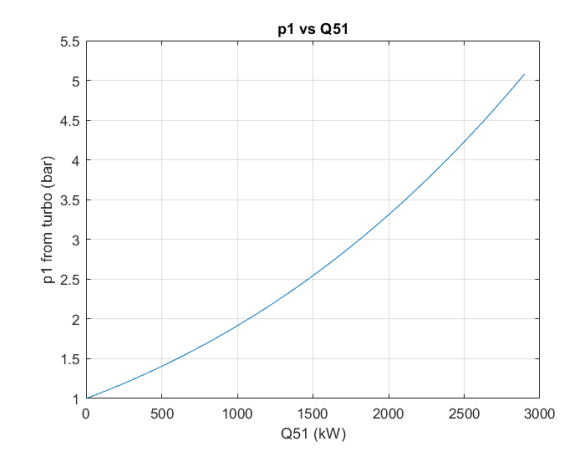


Figure 7.2: Open-water diagram for the propeller as implemented in Simulink

Figure 7.3: Inlet pressure as function of available turbo heat $(c_{tc} = 0.06)$

7.2 Engine selection and compression ratio

The engine selected for the simulation is the WINGD X82-2.0. This engine, also used by De Vos (2025), is a sufficient fit to the Duisburg Test Case vessel with respect to power output and engine speed. The engine is a two-stroke low-speed engine typically used in these types of vessel. The fuel rack must be limited to keep the engine from exceeding its maximum speed. This means that the Duisburg vessel will not be able to reach its full design speed of 25 knots. The most relevant engine data is shown in Table 7.1.

Table 7.1: Engine Data from WinGD (2024)

Engine power [kW @ 7 cylinders]	38500
Max engine speed [RPM]	84
Min engine speed [RPM]	58
Cylinders	7
sfc [g/Kwh @ MCR]	165.3

To create the engine model, the compression ratio is required to compute the Seiliger cycle. The compression ratio is based on the pressure data in Cui and Wang (2023) which was used for the ammonia calculations. The compression ratio was calculated with the thermodynamic formulas in section 6.5. An equation for p_{max} can be found (Equation 7.1). As q_{cv} and p_1 are functions of the simulation and cannot be simply directly calculated. Therefore, the compression ratio was tuned in the simulations to obtain the expected value for p_{max} . Another complication is the turbo model. As the pressures in Cui and Wang (2023) are almost linear, this turbo model results in a different correlation, which does not match the pressures at the 25,50,75% engine powers. This results in impossible high compression ratio's. Therefore, only the compression ratio of the 100% power is used, which is Rc = 12. This compression ratio matched a calculated pressure of $p_{max} = 20.4$ MPa with the literature value of $p_{max} = 19.9$ MPa. This value will be used further for this ICE.

$$p_{max} = p_1 * (Rc)^{\gamma_a} \cdot (\frac{q_{cv}}{Cv \cdot T_1 \cdot (Rc)^{\gamma_a - 1}} + 1)$$
 (7.1)

7.3 Case study setup and diesel fuel results

To show the results of the diesel engine, a case study is performed. The voyage selected for this ship is a single trip between the port of Hongkong and Rotterdam via the Suez canal. The trip consists of the following parts:

Part	Distance (km)	Speed (knots)
Hongkong -> Suez	12000	20
Suez canal	500	12
Suez -> Rotterdam	6200	20

Table 7.2: Case study voyage data

On the open water the ship will sail at 20 knots, whereas on the Suez canal the ship sails at 12 knots. The actual speed restriction in the Suez canal is 8 knots (El Amira co., 2025). Due to engine limitations and model constraints, the ship cannot move at this speed, while a speed of 12 knots is reachable for the vessel. The trial is set up as follows: The expected duration will be 21.5 days. The fuel rack is set so the speeds are reached. This is done for each configuration separately to obtain comparable results. This set-up results in Figure 7.4. In this figure, the fuel rack position is set to match the speed with the set values.

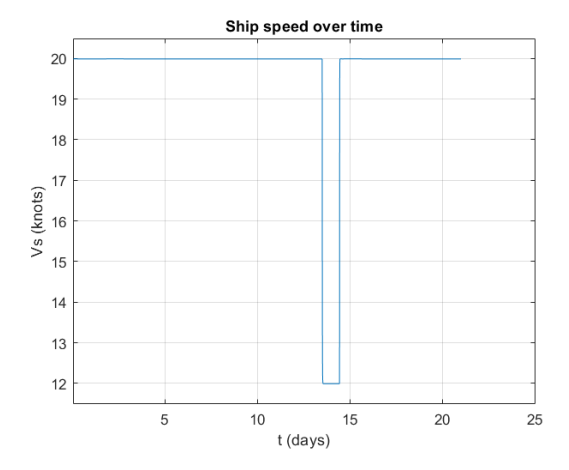


Figure 7.4: Sailing speed for diesel in the case study

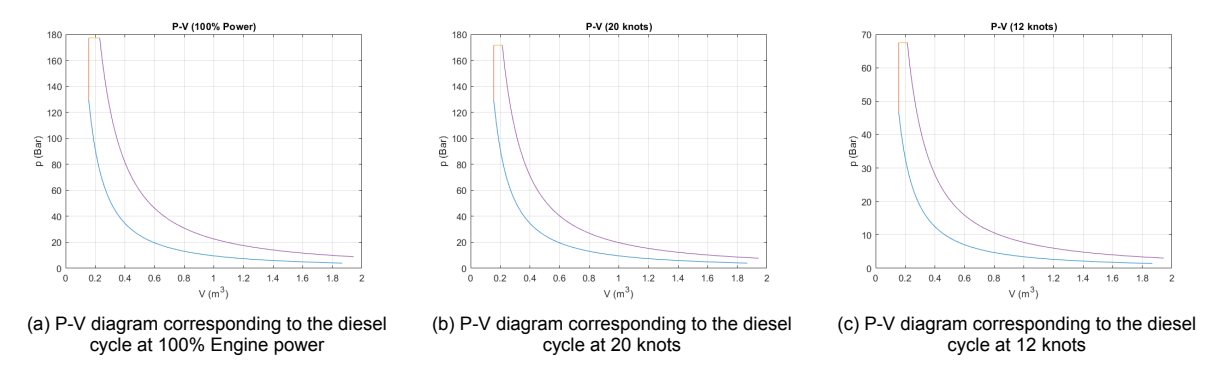


Figure 7.5: P-V diagrams for different engine loads with Diesel fuel

Figure 7.5 shows the P-V diagrams for the Duisburg sailing at 100% power and 20 and 12 knots respectably. At higher sailing speeds an higher peak pressure is reached than at 12 knots. Figure 7.6 shows the energy consumption, the fuel mass flow and the fuel consumed for this journey. The total fuel consumption is calculated to be 26500 tons. Based on simple calculations in Table 7.3, this is in agreement with the model.

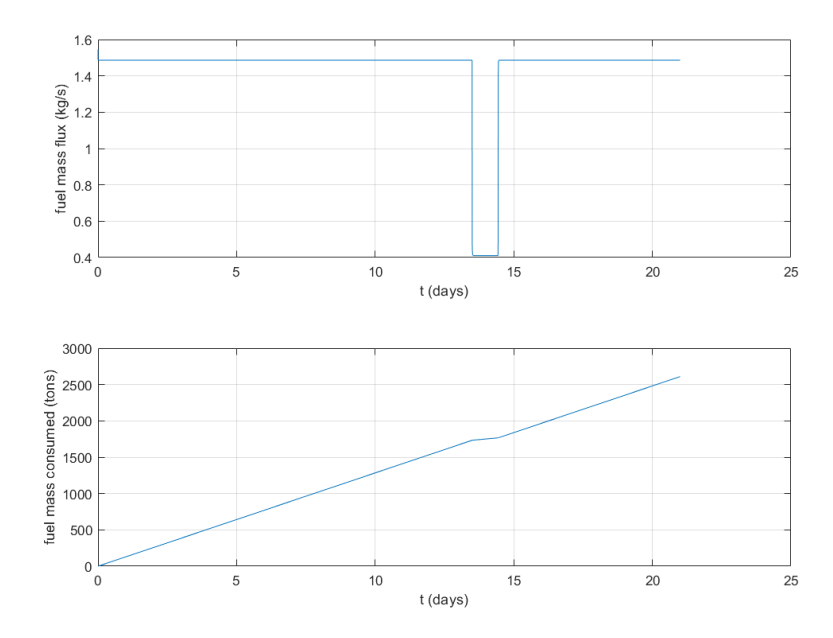


Figure 7.6: Energy and fuel consumption of the diesel model in the case study

Table 7.3: Fuel consumption verification

Engine efficiency at 20 knots [-]	0.43
Specific Fuel Consumption [g/kWh]	186
Engine power [kW]	27000
Estimated travel time [h]	514
Total energy consumed [kWh]	13880000
Total fuel consumed [ton]	2581

Figure 7.7 shows the resulting engine efficiency as a function of the set fuel rack. Here, it is shown that the overall engine efficiency increases with an increase in fuel rack and therefore engine power. The thermodynamic efficiency shows a negative correlation with respect to fuel rack, caused by a decreasing Heat division parameter. However, the increase in heat transfer efficiency and mechanical efficiency cause the overall efficiency to increase with the fuel rack.

The case study will continue in chapter 9.

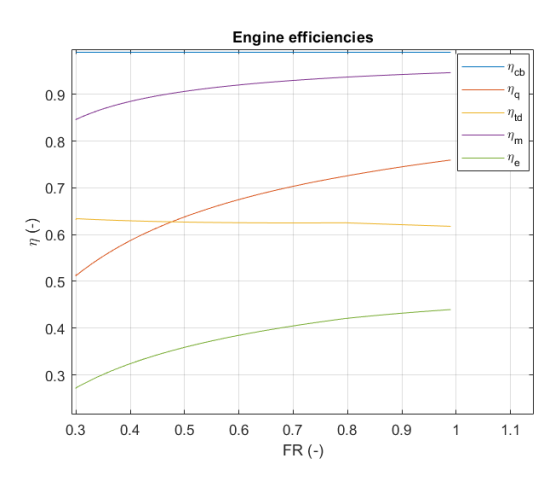


Figure 7.7: Efficiencies of the diesel engine as a function of Fuel Rack

Chapter 8

Alternative fuels model integration

This section will explain the influence of ammonia on the combustion process. This is based on the available literature. Changes from the diesel model will be made in the engine losses, such as the combustion losses, the heat transfer losses as well as the Seiliger parameters via the Heat division parameter *X*. The literature on ammonia and hydrogen will be explained in section 8.1 and 8.2. The changes to the Simulink model will be shown and explained in section 8.3.

8.1 Ammonia limitations in literature

The influence of ammonia on the combustion process is mainly based on 2 articles: X. Zhou et al. (2022) and Cui and Wang (2023). Both papers cover a part of the engine performance. Cui and Wang (2023) is based on experimental data with an ammonia energy percentage of 95% using standard diesel fuel as the pilot fuel. This data shows the influence of the engine load on the performance and is useful for computing the heat division parameter. X. Zhou et al. (2022), shows the heat balance at the different ammonia energy ratios and is useful for the estimation of combustion efficiency and the heat input efficiency.

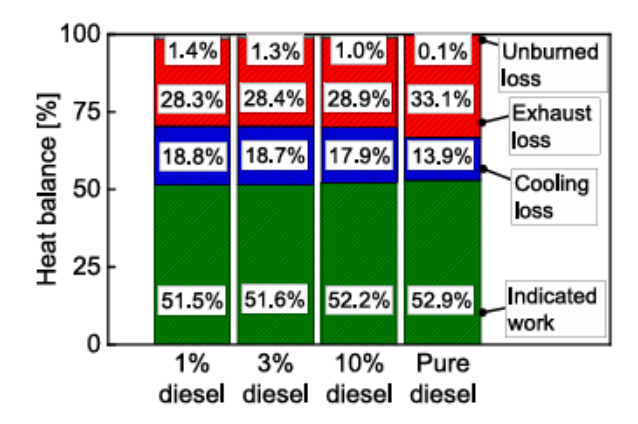
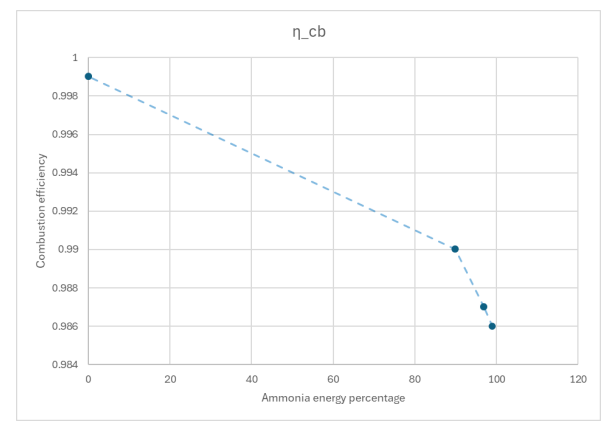


Figure 8.1: Simulation data from X. Zhou et al. (2022) shows the heat balance for different diesel energy percentages at constant engine speed and injected fuel energy

In the first place, the article of X. Zhou et al. (2022) will be analyzed. Figure 8.1 shows the heat balance based on a CFD simulation of a two-stroke low-speed ICE. The two important parts of this balance are the unburned loss and the cooling loss. Based on the flow of the calculations as defined in section 6.5, the cooling loss cannot be taken directly from this figure. Therefore, the data need more processing. In the first place, the combustion efficiency η_{cb} will be calculated, as this is the first step in the heat calculation. The other percentages are normalized to add up to 100% without the unburned losses. Now, the heat input efficiency η_q can be estimated for the different fuel ratios. With removal of the cooling loss, the remainder can be scaled back to 100% and as last, the thermodynamic efficiency η_{td}

can be calculated. The η_{td} cannot be used directly, as for this part the Seiliger cycle will be used, but can be kept as a reference for verification. The resulting graphs are shown in Figures 8.2 and 8.3. The result will be implemented in Simulink using linear lookup tables, resulting in a trend similar to that of these figures.



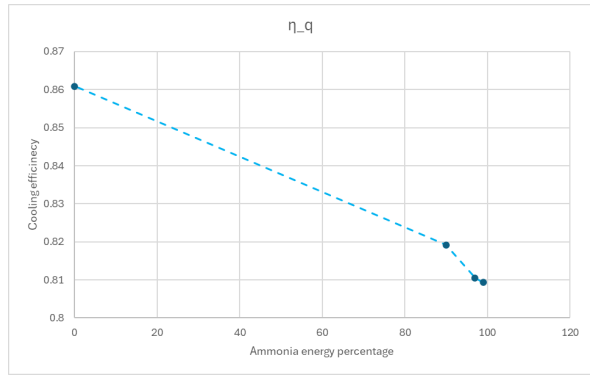


Figure 8.2: Combustion efficiency based on X. Zhou et al. (2022)

Figure 8.3: Heat input efficiency based η_q on X. Zhou et al. (2022). This efficiency includes all heat losses where energy does not work in the cylinder process.

The next step is to calculate the heat division parameter X. For this calculation, the data from Cui and Wang (2023) will be used. Cui and Wang (2023) shows the heat release rate for different loads of the engine at a constant ammonia energy ratio. This is shown in Figure 5.2. The data from these figures were processed from image to data using a digitizer tool. The resulting Heat Release Rate (HRR) [kJ/Ca] is integrated with the trapezoid rule to gain the energy added as a function of the crank angle (illustrated in Figure 8.4). The next step is to find how much heat is used for constant volume combustion and constant pressure combustion. For this project, all heat released before the peak in the HHR is assumed to be the constant volume heat and the remainder will be the constant pressure heat. With the calculated heats Q_{cp} and Q_{cp} , the heat division parameter X can be computed.

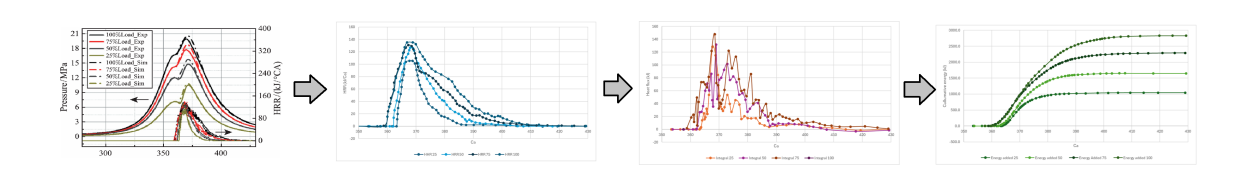
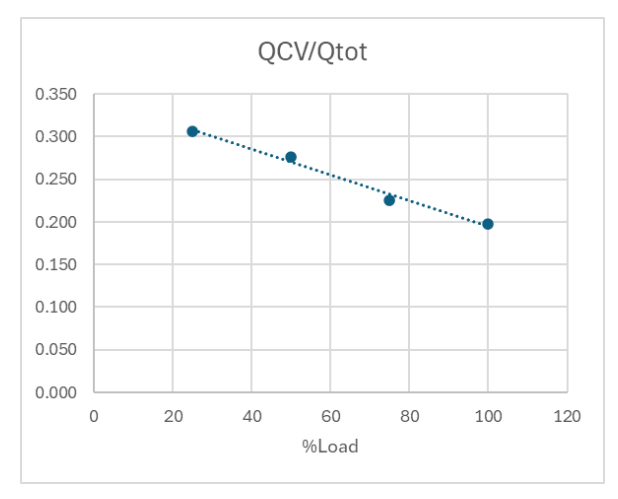


Figure 8.4: Illustration of the data processing, where data is extracted from a figure and processes into the total heat energy injected

Table 8.1: Engine data used by Cui and Wang (2023)

Parameter	100% Load	75% Load	50% Load	25% Load
Speed / rpm	103.0	94.0	82.2	65.3
Peak Pressure / MPa	19.93	17.73	14.75	10.5
Indicated Power / kW	9670	7355	4974	2580
Effective Power / kW	9010	6813	4560	2312



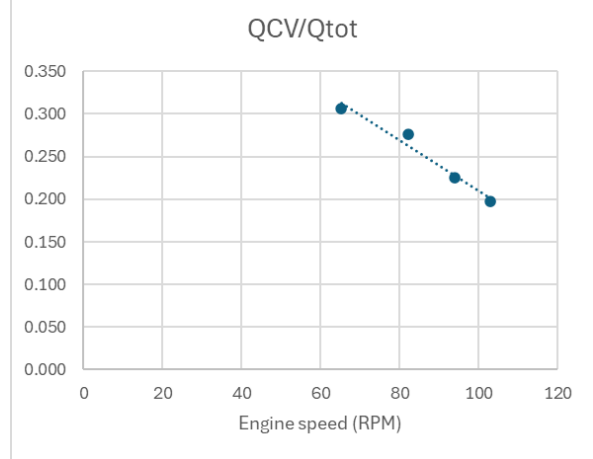


Figure 8.5: Heat Division parameter as a function of Engine load

Figure 8.6: Heat Division parameter as a function of Engine speed

The results are shown in Figure 8.5. This load on this engine was a propeller load. Using the engine speed available in Table 8.1, Figure 8.6 is created. Combining both figures shows in Figure 8.7 which result in a surface and is implemented in Simulink.

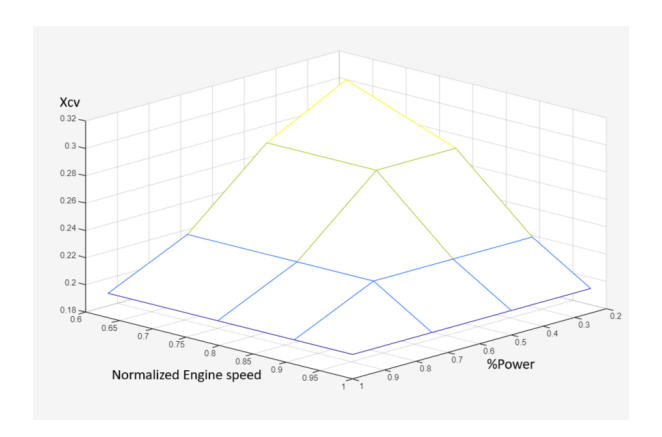


Figure 8.7: Heat division as a function of fuel rack and normalized engine speed derived with data from Cui and Wang (2023)

Finally, Equations 8.1 and 8.2 show the Lower Heating Value of the fuel mixture $h_{L,mix}$ and the stoichiometric air fuel ratio σ_{mix} . In these equations, AMR is the ammonia mass ratio of the mixture.

$$h_{L,mix} = AMR \cdot h_{L,amm} + (1 - AMR) \cdot h_{L,diesel}$$
(8.1)

$$\sigma_{mix} = AMR \cdot \sigma_{amm} + (1 - AMR) \cdot \sigma_{diesel}$$
 (8.2)

8.2 Hydrogen limitations in literature

The amount of literature available on diesel-hydrogen direct injection in two-stroke marine engines is rather limited. So, to build the hydrogen part of the model, more assumptions need to be made in combination with the available literature. The first point is the amount of Hydrogen Energy Ratio (HER). As hydrogen is an explosive fuel, a large amount of hydrogen can lead to high peak pressures in the cylinders with a high pressure. Several authors, under whom Serrano et al. (2021), use a maximum of 80% hydrogen energy. This HER will be used as a maximum in the model.

As with ammonia, different parts of the model need to be fitted to hydrogen. At first, the combustion losses need to be estimated. Several authors of the literature have focused on the losses that stem from the escape of hydrogen with the scavenging of the cylinder. Because they use port injection to bring hydrogen into the cylinder with the fresh air, during the phase where both intake and exhaust valves are opened, hydrogen will leak out with exhaust gases. Although these are commonly counted as unburned fuel and result in a lower combustion efficiency, this is not applicable to direct injection, as the exhaust valve will be closed when the fuel is injected and no hydrogen can escape. Therefore, it is assumed that hydrogen will combust with the same efficiency as diesel fuel, assuming a combustion efficiency of $\eta_{ch} = 0.999$ under nominal conditions, with a small reduction for a decrease in load.

The next step is the heat losses to the cylinder wall. The higher the engine speed, the less time heat has to transfer through the wall of the cylinder. Treacy et al. (2024) use a slower high-speed 4-stroke engine in simulation to test different injection strategies for efficiencies. They calculated the heat loss to be 10.9% at maximum load. Other authors, also using 4-stroke high-speed engines, have similar losses. Therefore, as no data are available on two-stroke slow speed, this is used as a starting point. When the engine speed decreases, more heat is expected to leak into the cylinder wall. The efficiency is decreased for the lower engine speeds based on this hypothesis.

The last part to consider is the heat division parameter. The source used to calculate this is De Haas (2025). De Haas assumes the scenarios of normal and fast hydrogen combustion at HER=0.8. The fast hydrogen combustion has the most in common with an otto cycle, where b = 1. Reverse engineering, using the provided temperatures, leads to a heat division factor of X=0.89. The normal hydrogen combustion computes to X=0.603. Fast hydrogen combustion is assumed to be the same as in low-load, slow-speed conditions, where the fuel has more time to combust at a constant volume. The normal combustion is assumed to correspond to high load, high speed conditions, where more fuel will be burned at constant pressure. The other values are interpolated with these values. It must be noted that De Haas uses low pressure injection, where hydrogen is mixed with air before combustion resulting in more pre-mix combustion. Therefore, questions must be raised about the appliance for high pressure direct injection.

8.3. Implementation 36

8.3 Implementation

The alternative fuels are implemented in Simulink to obtain the correct characteristics. A way to do this is by creating a specialized block that handles the change in fuel composition. The implementation of ammonia is shown in Figure 8.8. The block uses 2 incoming variables: The position of the fuel rack and the speed of the engine. The position of the fuel rack is an indication of the current engine power. The engine speed is normalized using the engine speed at MCR. With the fuel rack, the Ammonia Energy Ratio (AER) is found using a lookup table. The AER is used for the combustion and cooling losses. The data from section 8.1 is implemented in the lookup tables. However, to calculate the lower heating value and the stoichiometric air fuel ratio the Ammonia Mass Ratio (AMR) needs to be computed first. The last parameter to be implemented is the heat division parameter X, which depends on the normalized engine speed and the normalized engine power. The injection of ammonia fuel is adjusted to gain the same power output of the ICE for diesel-only case at nominal power.

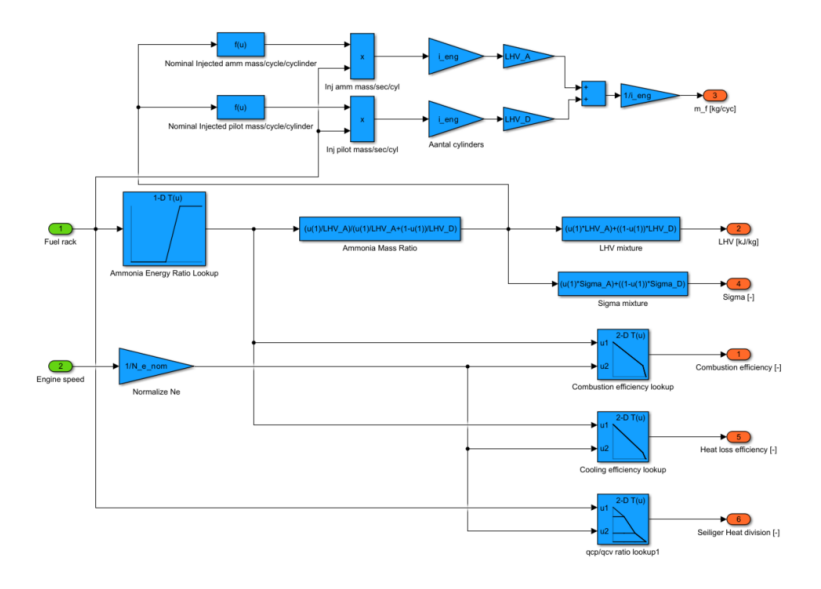


Figure 8.8: Changes to Simulink to incorporate the ammonia mixture

Hydrogen can be implemented similarly to ammonia. Here, there is hardly any influence of the HES as limited data was available. The hydrogen implementation is shown in Figure 8.9

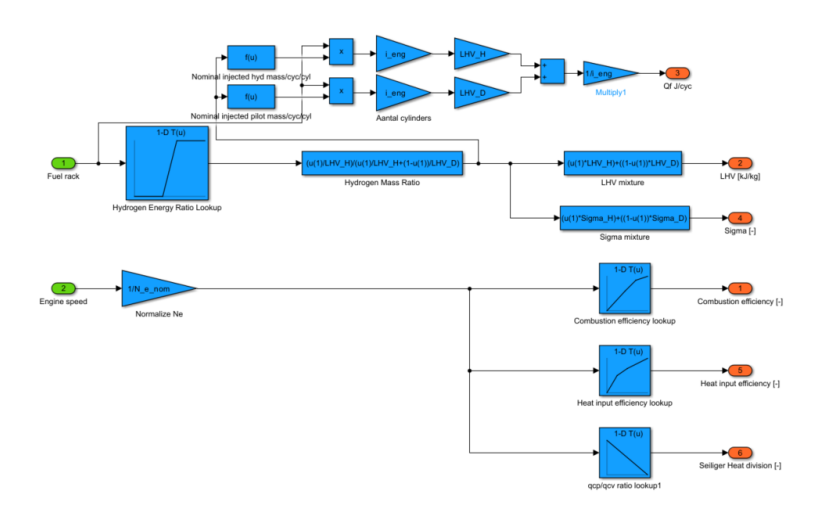


Figure 8.9: Changes to Simulink to incorporate the hydrogen mixture

8.3. Implementation 37

For the ammonia-diesel engine is chosen for a maximum AER of 95% at maximum power, as this multiple authors consider possible. For lower speeds, an AER of 80% is chosen to get more energy from easier combustible diesel fuel. The transition between the 2 AER is set between 0.5 and 0.7 FR. The AER as a function of the fuel rack is illustrated in Figure 8.10. For hydrogen, it is chosen to use a HER of 80% at maximum FR and a HER of 60% at lower FR. The HER is shown in Figure 8.11.

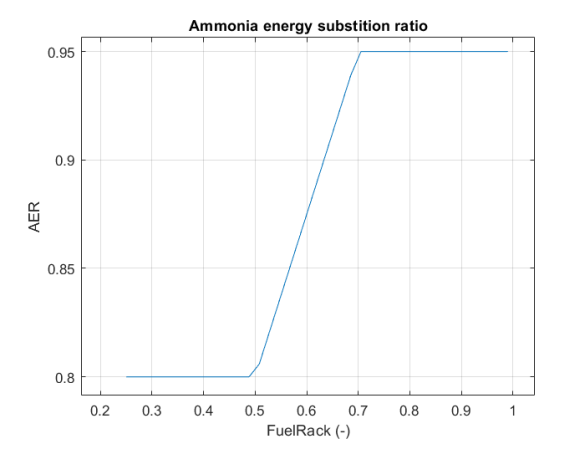


Figure 8.10: AER as function of Fuel rack

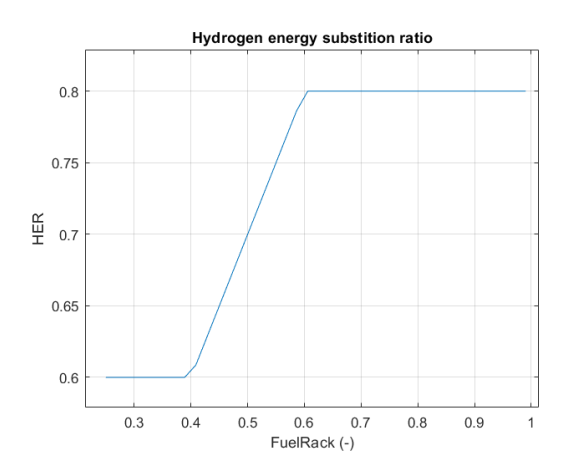


Figure 8.11: HER as function of Fuel rack

Chapter 9

Results

With the changes to the engine model completed, the results will be shown in this chapter. The results are divided into three parts: First, the application of Diesel-Ammonia fuel mixture, followed by the Diesel-Hydrogen fuel mixture. Finally, the results of the case study with the alternative fuel will be shown as a continuation of section 7.3.

9.1 Diesel-Ammonia

The literature on ammonia dual fuel combustion is used to update the model and has the largest influence on the changes in the model. The first to look at are the cooling losses. As derived from X. Zhou et al. (2022), the cooling loss is related to the ammonia energy percentage in the mixture. This behavior is also programmed into Simulink. Figure 9.1 shows the decrease in efficiency as the fuel rack increases at 0.5 < FR < 0.7. Although Figure 9.1 appears as a drastic step, the results are less pronounced than are expected at first glance. No engine speed-related behavior is programmed, which results in no change in heat transfer efficiency with the engine speed N_{ρ} .

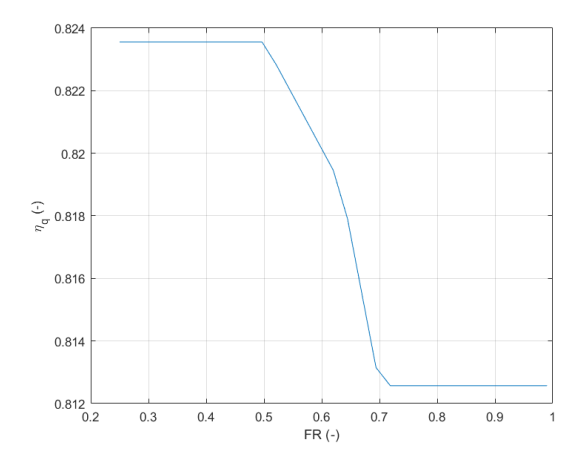


Figure 9.1: Heat input efficiency as function of fuel rack position

The second effect is shown in Figure 9.2. This figure shows the thermodynamic efficiency of the cycle as a function of engine speed and Fuel Rack. From this graph, it can be concluded that the thermodynamic efficiency η_{td} decreases with increasing Fuel Rack and engine speed. The effect of the fuel rack is the more pronounced factor with a greater decrease in efficiency than the engine speed. This is mainly related to the heat division parameter as described in section 8.1. An increase in engine load, and therefore fuel rack, leads to a decrease in q_{cv} . This is caused by the fact that more fuel is injected, which takes more time to combust, while a shorter time is available. This results in a lower part of the energy being released at constant volume and a higher part at constant pressure, which decreases

9.1. Diesel-Ammonia

the efficiency of the thermodynamic cycle. A similar point can be made about the relation with speed, where at a higher speed, the fuel has a shorter time to combust at a constant volume.

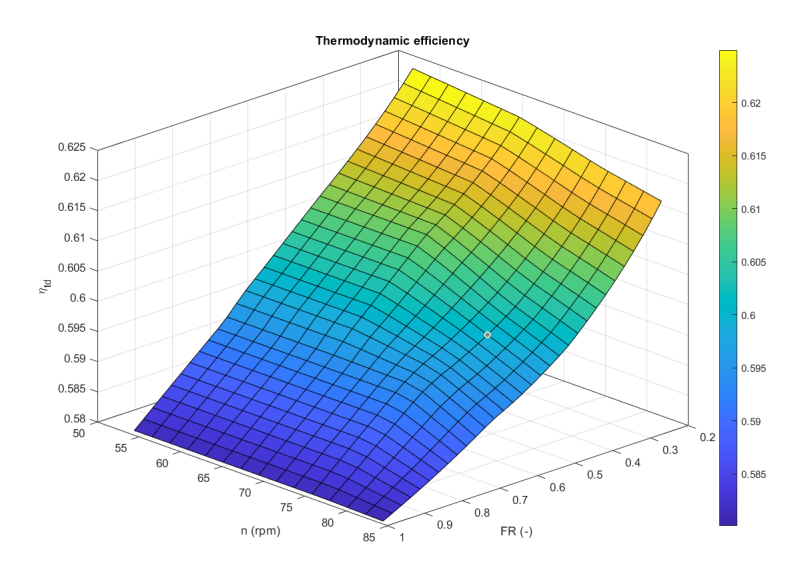


Figure 9.2: Thermodynamic efficiency as function of engine speed and fuel rack position

The last important result is the total engine efficiency η_e . This is shown in Figure 9.3. This surface contains all the effects of ammonia-diesel combustion. There are several important remarks to make on this graph. The first is the overall drop in efficiency at lower engine loads. This effect is explained by low mechanical efficiency at lower speeds, as can also be seen in the breakdown in Figure 9.4. A second drop and non-linearity can be seen at FR=0.7. This drop is caused by an increase in heat transfer losses, as shown in Figure 9.1. The final note is the effect of increasing the engine speed. The overall efficiency drops when the Fuel Rack is kept constant, but this is related to both friction losses that increase with engine speed and a decrease in thermodynamic efficiency, as can be seen in Figure 9.2.

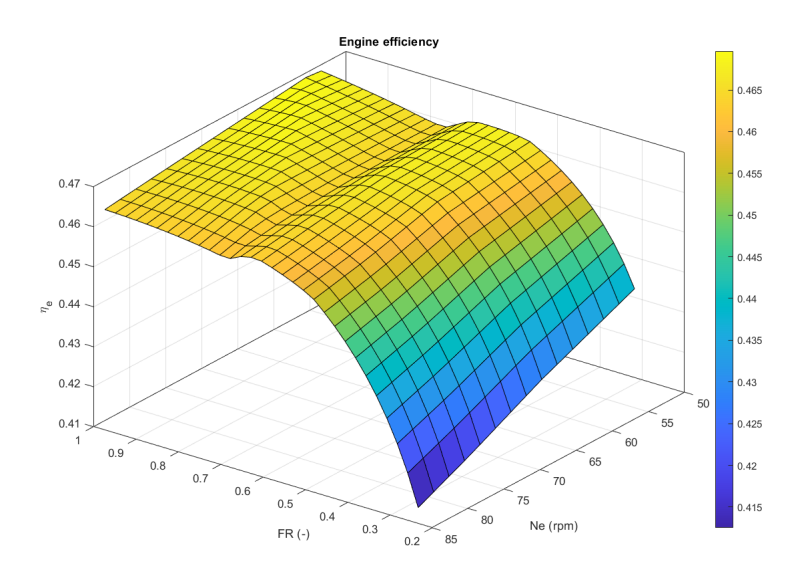


Figure 9.3: Engine efficiency as function of engine speed and fuel rack position

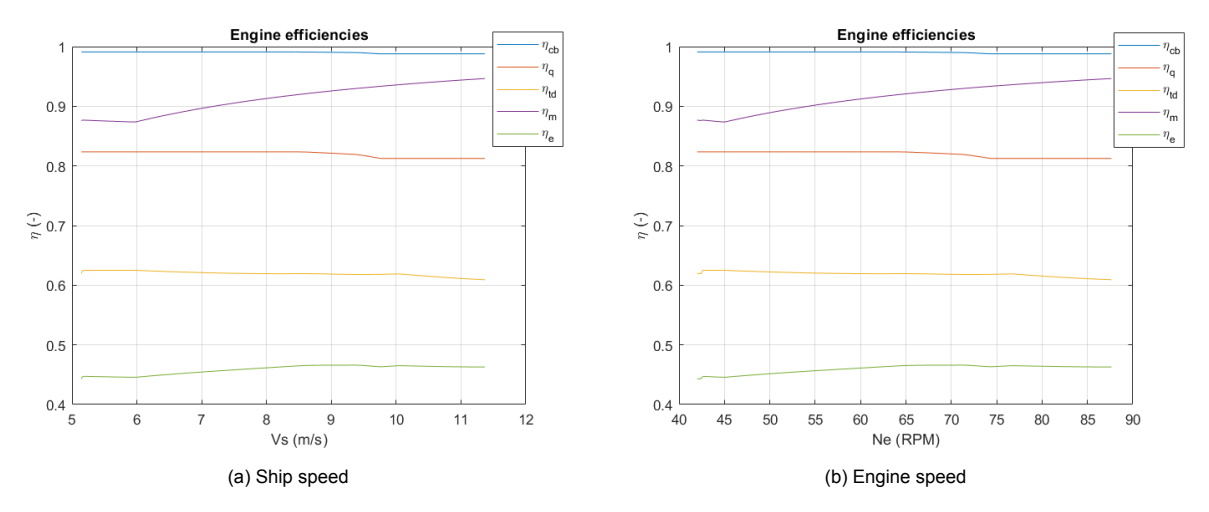


Figure 9.4: Engine efficiencies as functions of different parameters under propeller load

Finally, the corresponding P-V diagrams are shown in Figure 9.5. Compared to the diesel fuel case, the peak pressure at maximum power is lower when the diesel-ammonia mixture is used. The same holds for the maximum pressure at 20 and 12 knots. This can be explained by the heat division parameter being lower for diesel-ammonia mode than for diesel-only mode, which results in less of the heat added during constant volume, with as a result a lower peak pressure.

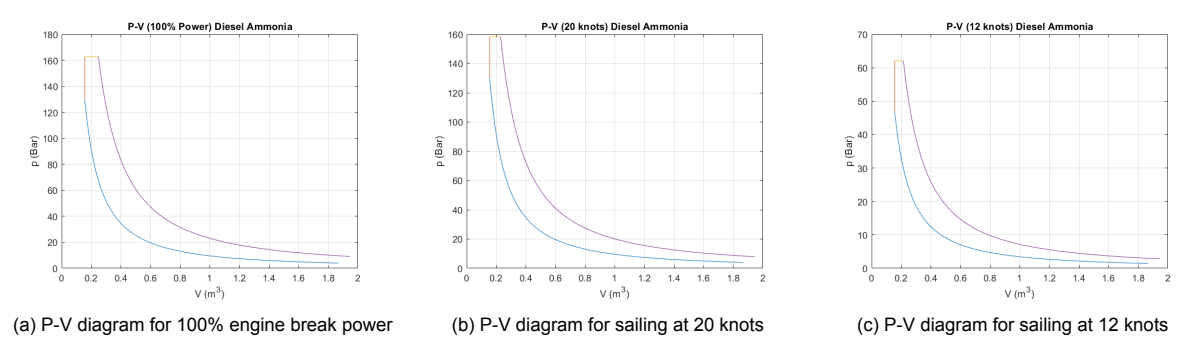


Figure 9.5: P-V diagram for different engine loads with Diesel-Ammonia fuel

9.2 Diesel-Hydrogen

This section will discuss the results of the hydrogen-diesel fuel mixture. These effects can be seen in Figure 9.7 and 9.8. In Figure 9.6, the resulting heat division parameter can be seen as a function of the engine speed. As described in section 8.2, the values are interpolated between a fast hydrogen combustion at a very low speed and a normal hydrogen combustion at the maximum engine speed. The resulting thermodynamic efficiency can be seen in Figure 9.8. The thermodynamic efficiency is 64% and shows a very small decrease with an increase in speed and load. The effect can be prescribed to the higher added heat at constant volume, which increases the thermodynamic efficiency, as well as the compression ratio, not commonly not high for hydrogen engines due to explosion risks. The heat input efficiency and combustion efficiency are shown in Figure 9.7. Their behavior is programmed as explained in section 8.2. The overall engine efficiency is predicted to increase with increasing ship speed, but this is mostly related to mechanical efficiency and heat input efficiency as the thermodynamic efficiency keeps constant.

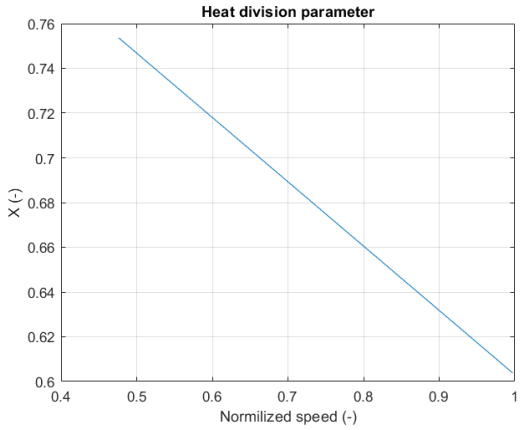


Figure 9.6: Heat division parameter *X* as function of the

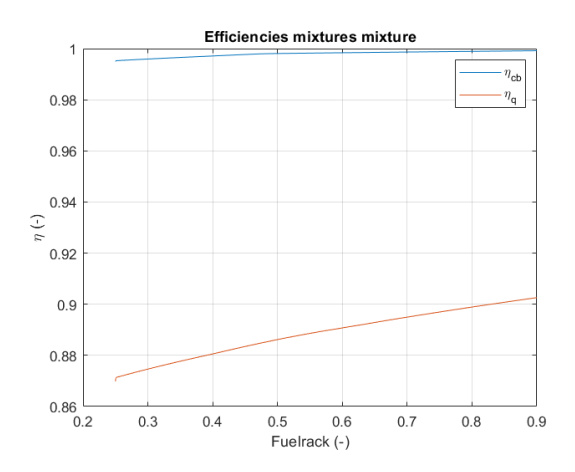
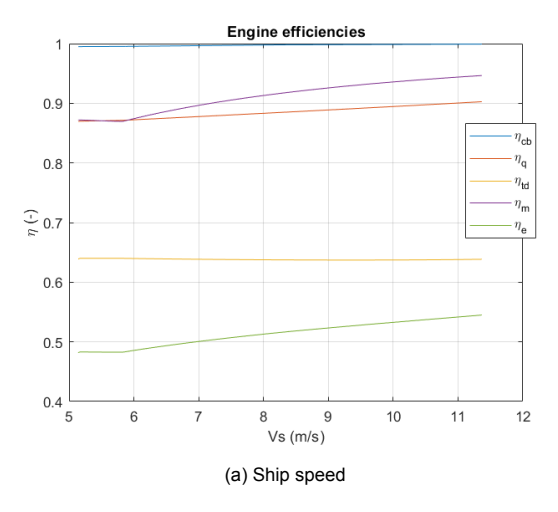


Figure 9.7: Combustion efficiency η_{cb} and heat input efficiency η_q as a function of engine speed



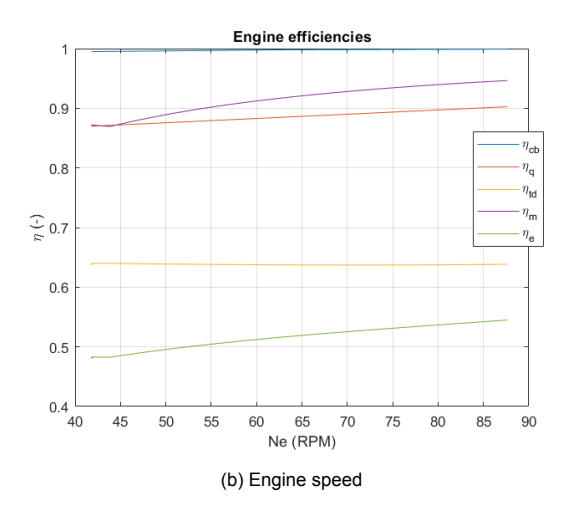
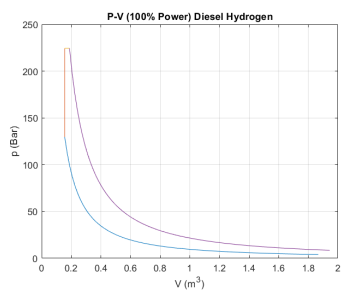
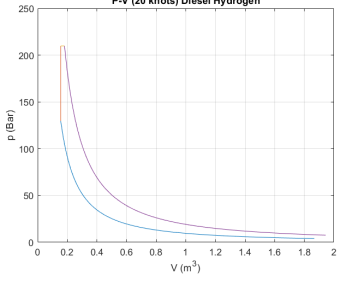
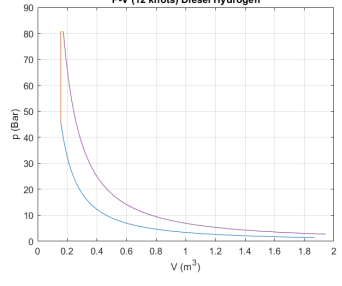


Figure 9.8: Engine efficiencies as functions of different parameters under accelerating propeller load

To close the section on diesel-hydrogen fuel, the P-V diagrams at different load points are shown in Figure 9.9. The engine pressures generated by the diesel-hydrogen combustion are larger than the diesel only case for all P-V diagrams. This is explained by the high heat division parameter, which results in a higher Seiliger parameter a (Equation 6.20), which results in a higher peak pressure (Equation 6.23).







(a) P-V diagram for 100% engine break power

(b) P-V diagram for sailing at 20 knots

(c) P-V diagram for sailing at 12 knots

Figure 9.9: P-V diagram for different engine loads with Diesel-Hydrogen fuel

9.3 Case study (continuation)

With the engine models adjusted for ammonia and hydrogen, the case study can be continued. The setup of the case study is explained in section 7.3. The ship will sail at 20 and 12 knots, which is confirmed in Figure 9.10.

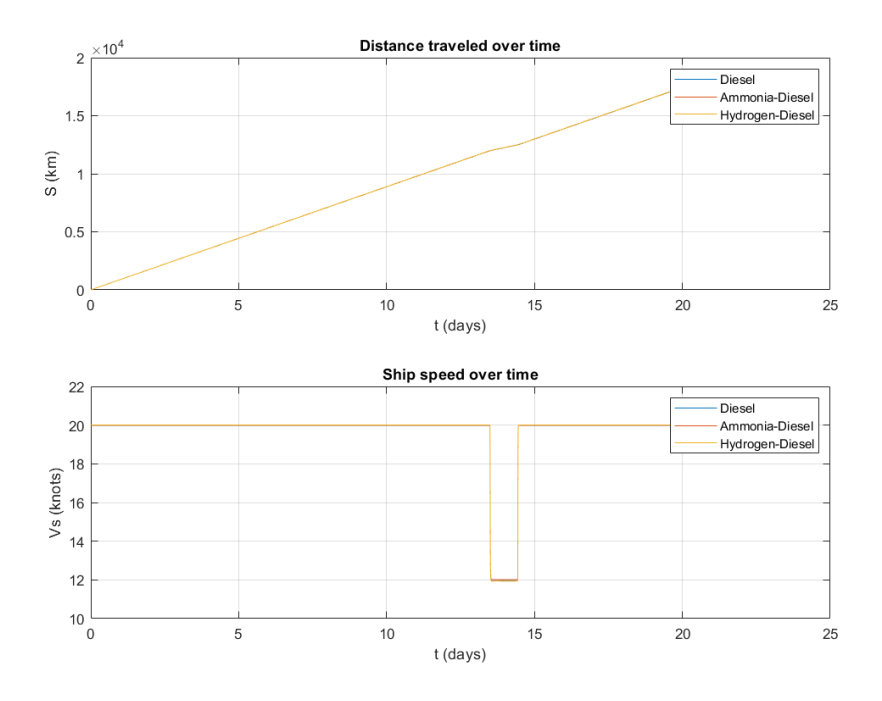


Figure 9.10: Voyage results for the different fuel configurations

The results of the fuel consumption of the voyage are shown in Figure 9.11. Separate fuel mixtures can also be found in Appendix B. In the first subgraph as well as Figure 9.12, the energy flow is depicted for all fuels. The energy consumption of the diesel-only mode is the highest, followed by the ammonia-diesel mode and finally the hydrogen-diesel mode. The engine break power is constant to keep the ship speed constant. The effect can be explained by the overall efficiency of the engine. The model predicts that the hydrogen-diesel mode has the highest efficiency, while the diesel-only mode has the lowest efficiency. This effect is also shown at the slower speed of sailing, where the consumption of diesel-only energy is again the highest. Therefore, a diesel-hydrogen engine would be the most feasible in terms of efficiency for future applications based on this simulation.

The second graph shows the mass flow for the fuel configurations, where the separation is made between the main fuel and the pilot fuel. The ammonia fuel mass flow is higher than the diesel mass flow. This effect is related to the lower heating values of the different fuels, where more mass of ammonia is necessary to keep the same amount of chemical energy as for diesel fuel. Based on the LHV, Diesel contains 2.29 times the energy of ammonia per kg. This can also be seen for the hydrogen fuel as its higher LHV results in less hydrogen mass flow. Therefore, a ship will need to carry much more mass and volume of ammonia fuel in dual fuel mode, than diesel in the diesel-only. This can be a problem when converting vessels to alternative fuels. And while the hydrogen mass necessary to fuel the ship is a lot smaller than diesel, the volume required for this hydrogen will be more. This is related to the storage density and the storage conditions.

It can also be noted in this graph that the pilot fuel mass is about the same for the hydrogen fuel mass as the combination of LHV and energy share. The effect of ammonia energy share is also visible at the lower speed part. The ammonia fuel flow comes relatively closer the diesel fuel flow as a result in the drop in ammonia energy share, which increases the diesel energy in the mixture at lower speeds. A similar effect can also be seen for hydrogen. It is important to note that the uncertainty in the overall

literature data can influence engine performance and fuel consumption. However, it has not been determined how this impacts the engine.

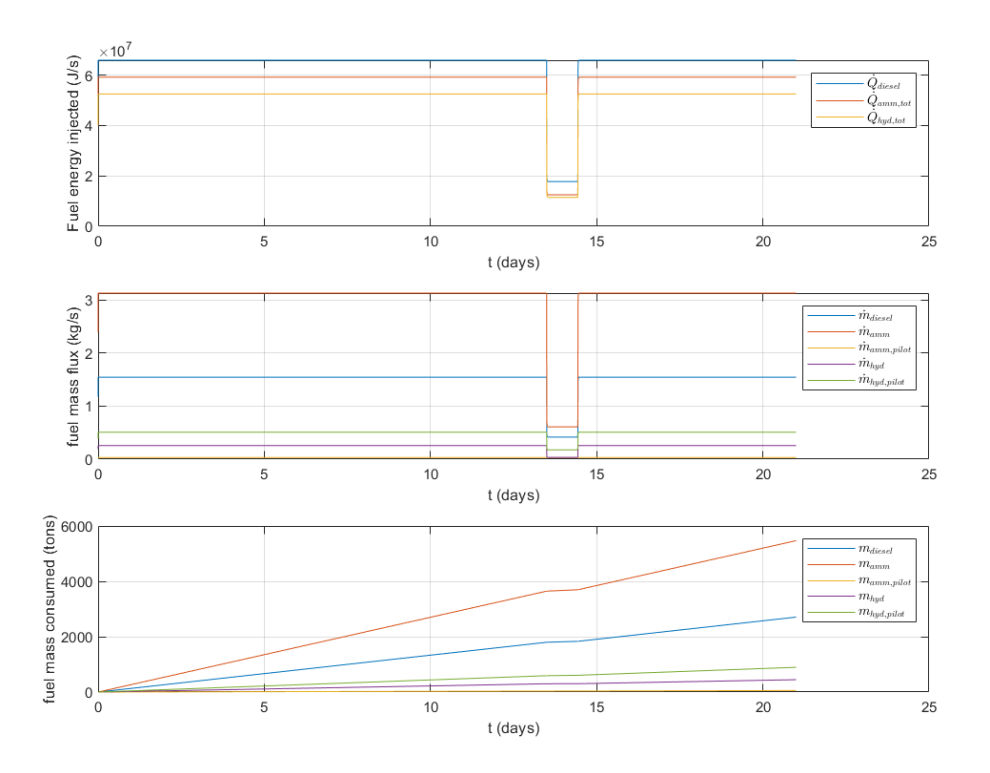


Figure 9.11: Fuel consumption results for the voyage

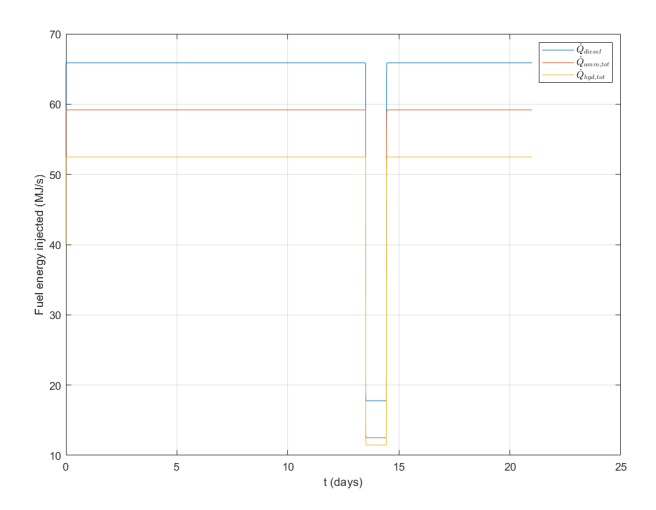


Figure 9.12: Total Energy flow for all three fuel-mixtures

Chapter 10

Conclusion

How can an ICE be modeled to use diesel, diesel-ammonia, and diesel-hydrogen to show the effects of these fuels in voyage simulations?

This thesis presents an approach to modeling a post-Panamax container ship powered by ammoniadiesel and hydrogen-diesel dual-fuel configurations. By implementing simulation in MATLAB Simulink, this work integrates a hydrodynamic model, an internal combustion engine model in an effort to model the complexities of alternative fuel behavior. The answers to the research sub-questions are summarized below:

· How can the hydrodynamic part and the ICE of the simulation be modeled?

The hydrodynamic behavior of the vessel is modeled by dividing the system into resistance, propeller, and shaft dynamics blocks. Resistance is calculated using empirical formulas based on the Duisburg Test Case, incorporating friction via the ITTC 1957 method and form factors from CFD. Propeller behavior is characterized using open-water diagrams and quadratic curve fits to thrust and torque coefficients. The dynamics of the shaft and the ship is modeled through force and torque balance equations, integrated to obtain RPM and speed. The ICE is modeled on the basis of the Seiliger cycle. Therefore, the different stages are integrated in the Simulink model, as well as the heat input and the turbo model. The model incorporates the common losses found in internal combustion engines.

How can the influence of ammonia be modeled for the simulator?

The influence of ammonia is modeled by modifying the fuel-related parameters within the engine block to reflect ammonia's characteristics. As shown in section 8.1, ammonia affects combustion behavior and engine performance. These effects are captured in the model by adjusting combustion efficiency, cooling losses, and the Seiliger heat division parameter based on literature. The results of the effects of ammonia are shown in section 9.1. When comparing the diesel-ammonia fuel in the voyage simulator, it is found that the ammonia produces lower peak pressures as well as consuming more fuel mass than the diesel-only case.

• How can the hydrogen literature be applied for the simulator?

Hydrogen's behavior is integrated into the simulator by using literature-derived relationships for its thermodynamic and combustion properties. The model adjusts the Seiliger parameters to account for more rapid combustion as well as the losses in unburned fuel and the heat input. These behaviors are visible in the simulation results in section 9.2. In the voyage simulation, it is shown that the required hydrogen fuel mass will be smaller than the diesel fuel mass in diesel-only case and results in higher peak pressures in the P-V diagrams when again compared to the diesel-only case.

Chapter 11

Discussion and recommendations

In hindsight, several discussion points need to be brought up. First, there are limitations to the Duisburg data. As the ship was only tested at the higher design speeds, this results in a lack of data at the slower sailing speeds. This can be defended by arguing that the ship is only going to be used around design speeds. However, the lack of low-speed data means that resistance behavior at these speeds is absent. It would be recommended to retest the Duisburg model at these speeds or to use another vessel where these data are known.

Second, there is the reliability of the digitizer results. A change in the selection of points on the heat release curves would cause a change in the heat division parameter. As the data were noisy, the results may not be fully trusted.

Third, there are concerns about the use of the fuel rack position (FR) as a measurement of the relative engine power. Although it is true that it is related to the injected fuel and the resulting power, the FR can change instantly while the engine has a wind up to reach the new power output. Relying on FR alone as a power measure can result in misleading interpretations, especially during transient or unstable operating conditions. Therefore, it would be suggested to use the real power output of the engine for further research to link back to the alternative fuel properties.

Fourth, there is the availability of data on the behavior of alternative fuels in these specific engines. Limited research is done on hydrogen-diesel specifically but also ammonia-diesel. Hence, it would be recommended to either perform the required experiments or simulations to get a further understanding on the dynamics of the alternative fuels.

Lastly, there is the issue on the alternative energy share. There is no current literature on the energy share and how it is related to engine conditions. Although it can be expected that for lower engine loads, more pilot fuel can be used to gain more stable conditions, no real research has been done on this topic. Therefore, further research on this topic is recommended. The energy share in Figure 8.10 and 8.11 are assumptions based on the general idea that ammonia could reach a 95% energy ratio and hydrogen 80% energy ratio. The transition phase is mainly used to show the effect of the programmed behavior of the engine and is also an assumption.

Bibliography

- Alberer, D., Hjalmarsson, H., & Re, L. (2011). *Identification for automotive systems*. Springer London. https://doi.org/10.1007/978-1-4471-2221-0
- Bassam, A. (2017, June). Use of voyage simulation to investigate hybrid fuel cell systems for marine propulsion. https://eprints.soton.ac.uk/412705/
- Chen, S. K., & Flynn, P. F. (1965). Development of a single cylinder compression ignition research engine. SAE technical papers on CD-ROM/SAE technical paper series. https://doi.org/10.4271/650733
- Coppo, M. (2023). Powering a greener future: The omt injector enables high-pressure injection of ammonia and methanol.
- Cui, L., & Wang, H. (2023). Simulation Research on the Combustion of Marine Low-Speed Ammonia Engine. *JOURNAL OF ENGINEERING THERMOPHYSICS*, 44(11).
- De Haas, T. (2025). Hydrogen combustion in marine two-stroke engines using LPDI.
- De Vos, P. (2020). AmmoniaDrive: a solution for zero-emission shipping?! SWZ Maritime, 141(3), 36–37. https://repository.tudelft.nl/islandora/object/uuid%3A348fb3d1-2ad7-43f1-b8b2-28dfd1139a88
- De Vos, P. (2025). Preliminary implementation of a fc-ice system for power and propulsion of a 14,000 teu container ship.
- De Vries, N. (2019). Safe and effective application of ammonia as a marine fuel. https://resolver.tudelft.nl/uuid:be8cbe0a-28ec-4bd9-8ad0-648de04649b8
- Dere, C. (2023, January). *Hydrogen as a transition fuel in marine engines*. https://doi.org/10.1007/978-3-031-30171-1\{_}}58
- Di Blasio, G., Agarwal, A. K., Belgiorno, G., & Shukla, P. C. (2021, December). *Clean fuels for mobility*. Springer Singapore. https://doi.org/10.1007/978-981-16-8747-1
- Ding, Y., Stapersma, D., & Grimmelius, H. (2012). Using parametrized finite combustion stage models to characterize combustion in diesel engines. *Energy & Fuels*, *26*(12), 7099–7106. https://doi.org/10.1021/ef3014212
- Ding, Y., Xiang, L., Li, J., Cui, H., & Zhang, Y. (2018). Modeling of thermodynamic properties of diesel fuel and In-Cylinder gas for diesel engine combustion investigation. *Energy & Fuels*, 32(12), 12871–12883. https://doi.org/10.1021/acs.energyfuels.8b02570
- El Amira co. (2025). Suez Canal | El Amira. https://elamira.com/services/suez-canal/
- El-Gohary, M. M. (2009). Design of marine hydrogen internal combustion engine. *Alexandria Engineering Journal*, 48(1), 57–65.
- Finger, G. (2021). Simplified calculation of friction mean effective pressure for fast simulation of fuel consumption. *SN Applied Sciences*, *4*(1). https://doi.org/10.1007/s42452-021-04892-y
- Heywood, J. (2018). Internal Combustion Engine Fundamentals 2E. McGraw Hill Professional.
- Kumar Agarwal, A., & Valera, H. (2021, December). *Greener and scalable e-fuels for decarbonization of transport*. Springer Singapore. https://doi.org/10.1007/978-981-16-8344-2
- Lesmana, H., Zhang, Z., Li, X., Zhu, M., Xu, W., & Zhang, D. (2019). NH3 as a transport fuel in internal combustion Engines: A technical review. *Journal of Energy Resources Technology*, *141*(7). https://doi.org/10.1115/1.4042915
- Lewandowski, M. T., Pasternak, M., Haugsvær, M., & Løvås, T. (2023). Simulations of ammonia spray evaporation, cooling, mixture formation and combustion in a direct injection compression ignition engine. *International Journal of Hydrogen Energy*, *52*, 916–935. https://doi.org/10.1016/j.ijhydene.2023.06.143

Bibliography 47

Ley, M. B., Jepsen, L. H., Lee, Y.-S., Cho, Y. W., Von Colbe, J. M. B., Dornheim, M., Rokni, M., Jensen, J. O., Sloth, M., Filinchuk, Y., Jørgensen, J. E., Besenbacher, F., & Jensen, T. R. (2014). Complex hydrides for hydrogen storage – new perspectives. *Materials Today*, *17*(3), 122–128. https://doi.org/10.1016/j.mattod.2014.02.013

- Li, H., Cao, X., Liu, Y., Shao, Y., Nan, Z., Teng, L., Peng, W., & Bian, J. (2022). Safety of hydrogen storage and transportation: An overview on mechanisms, techniques, and challenges. *Energy Reports*, *8*, 6258–6269. https://doi.org/10.1016/j.egyr.2022.04.067
- Livanos, G., & Kyrtatos, N. P. (2006). A model of the friction losses in diesel engines. SAE technical papers on CD-ROM/SAE technical paper series. https://doi.org/10.4271/2006-01-0888
- Miedema, S., & Lu, Z.-H. (2002). The dynamic behavior of a diesel engine.
- Moctar, O. E., Shigunov, V., & Zorn, T. (2012). Duisburg Test case: Post-Panamax container ship for benchmarking. *Ship Technology Research*, *59*(3), 50–64. https://doi.org/10.1179/str.2012.59. 3.004
- Murphy, A., Norman, A., Pazouki, K., & Trodden, D. (2015). Thermodynamic simulation for the investigation of marine Diesel engines. *Ocean Engineering*, *102*, 117–128. https://doi.org/10.1016/j.oceaneng.2015.04.004
- Osman, A. I., Mehta, N., Elgarahy, A. M., Hefny, M., Al-Hinai, A., Al-Muhtaseb, A. H., & Rooney, D. W. (2021). Hydrogen production, storage, utilisation and environmental impacts: a review. *Environmental Chemistry Letters*, 20(1), 153–188. https://doi.org/10.1007/s10311-021-01322-8
- Park, C., Jang, Y., Jang, I., Kim, M., & Kim, Y. (2024). Combustion and emission characteristics of high-pressure ammonia direct injection marine dual-fuel engine. *Fuel*, *385*. https://doi.org/10.1016/j.fuel.2024.134110
- Pipitone, E. (2009). A new simple friction model for S. I. engine. SAE technical papers on CD-ROM/SAE technical paper series. https://doi.org/10.4271/2009-01-1984
- Rakopoulos, C. D., & Giakoumis, E. G. (2006). Review of Thermodynamic Diesel Engine Simulations under Transient Operating Conditions. *SAE technical papers on CD-ROM/SAE technical paper series*. https://doi.org/10.4271/2006-01-0884
- Reiter, A. J., & Kong, S.-C. (2010). Combustion and emissions characteristics of compression-ignition engine using dual ammonia-diesel fuel. *Fuel*, *90*(1), 87–97. https://doi.org/10.1016/j.fuel.2010. 07.055
- Sapra, H., Godjevac, M., De Vos, P., Van Sluijs, W., Linden, Y., & Visser, K. (2020). Hydrogen-natural gas combustion in a marine lean-burn SI engine: A comparitive analysis of Seiliger and double Wiebe function-based zero—dimensional modelling. *Energy Conversion and Management*, 207, 112494. https://doi.org/10.1016/j.enconman.2020.112494
- Seddiek, I. S., El-gohary, M. M., & Ammar, N. R. (2015). The hydrogen-fuelled internal combustion engines for marine applications with a case study. *DOAJ (DOAJ: Directory of Open Access Journals)*. https://doaj.org/article/3a5e85b9e31f403b86643fd042af80f7
- Serrano, J., Jiménez-Espadafor, F., & López, A. (2019a). Analysis of the effect of different hydrogen/diesel ratios on the performance and emissions of a modified compression ignition engine under dual-fuel mode with water injection. Hydrogen-diesel dual-fuel mode. *Energy*, 172, 702—711. https://doi.org/10.1016/j.energy.2019.02.027
- Serrano, J., Jiménez-Espadafor, F., & López, A. (2019b). Analysis of the effect of the hydrogen as main fuel on the performance of a modified compression ignition engine with water injection. *Energy*, 173, 911–925. https://doi.org/10.1016/j.energy.2019.02.116
- Serrano, J., Jiménez-Espadafor, F., & López, A. (2021). Prediction of hydrogen-heavy fuel combustion process with water addition in an adapted low speed two stroke diesel engine: Performance improvement. *Applied Thermal Engineering*, 195, 117250. https://doi.org/10.1016/j.applthermaleng.2021.117250
- Shi, W. (2013). Dynamics of Energy System Behaviour and Emissions of Trailing Suction Hopper Dredgers.
- Song, M., Wang, Q., Wang, Z., Fang, Y., Qu, W., Gong, Z., & Feng, L. (2024). Auto-ignition characteristics and chemical reaction mechanism of ammonia/n-heptane mixtures with low n-heptane content. *Fuel*, *364*, 131011. https://doi.org/10.1016/j.fuel.2024.131011
- Stapersma, D. (2010). Lecture notes: Diesel Engines Volume 1 Performance Analysis. NLDA & Delft UT.

Bibliography 48

Sui, C. (2021). Energy Effectiveness and Operational Safety of Low-Powered Ocean-going Cargo Ship in Various (Heavy) Operating Conditions.

- Sui, C., De Vos, P., Stapersma, D., Visser, K., & Ding, Y. (2020). Fuel Consumption and Emissions of Ocean-Going Cargo Ship with Hybrid Propulsion and Different Fuels over Voyage. *Journal of Marine Science and Engineering*, 8(8), 588. https://doi.org/10.3390/jmse8080588
- Sui, C., Song, E., Stapersma, D., & Ding, Y. (2017). Mean value modelling of diesel engine combustion based on parameterized finite stage cylinder process. *Ocean Engineering*, *136*, 218–232. https://doi.org/10.1016/j.oceaneng.2017.03.029
- Treacy, M., Hadadpour, A., Bai, X.-S., & Fatehi, H. (2024). Performance and emissions of a novel high-pressure direct injection hydrogen dual-fuel engine. *Fuel*, *376*, 132639. https://doi.org/10.1016/j.fuel.2024.132639
- Van Duijn, J. (2021, January). Modelling diesel-ammonia two-stroke engines. https://repository.tudelft.nl/islandora/object/uuid%3A2be63cac-85e7-4367-99a8-e811e3248936
- Vrijdag, A., Stapersma, D., & Van Terwisga, T. (2009). Systematic modelling, verification, calibration and validation of a ship propulsion simulation model. *Journal of Marine Engineering & Technology*, 8(3), 3–20. https://doi.org/10.1080/20464177.2009.11020223
- Wang, L., Liu, D., Yang, Z., Li, H., Wei, L., & Li, Q. (2018). Effect of H2 addition on combustion and exhaust emissions in a heavy-duty diesel engine with EGR. *International Journal of Hydrogen Energy*, 43(50), 22658–22668. https://doi.org/10.1016/j.ijhydene.2018.10.104
- WinGD. (2024, June). X82-2.0 Data sheet. https://wingd.com/media/30ihszux/x82-2-0_20240626_ 1041.pdf
- Woud, H. K., & Stapersma, D. (2002, January). *Design of propulsion and electric power generation systems*. Witherby Publishing Group Ltd. http://ci.nii.ac.jp/ncid/BA64216262
- Wu, Q., Liang, X., Zhu, Z., Cui, L., & Liu, T. (2024). Numerical Simulation Research on combustion and emission characteristics of Diesel/Ammonia Dual-Fuel Low-Speed Marine Engine. *Energies*, 17(12). https://doi.org/10.3390/en17122960
- Yousefi, A., Guo, H., Dev, S., Liko, B., & Lafrance, S. (2021). Effects of ammonia energy fraction and diesel injection timing on combustion and emissions of an ammonia/diesel dual-fuel engine. *Fuel*, *314*. https://doi.org/10.1016/j.fuel.2021.122723
- Zhang, Z., Long, W., Dong, P., Tian, H., Tian, J., Li, B., & Wang, Y. (2022). Performance characteristics of a two-stroke low speed engine applying ammonia/diesel dual direct injection strategy. *Fuel*, 332. https://doi.org/10.1016/j.fuel.2022.126086
- Zhou, J., & Wang, H. (2020). Study on efficient removal of SOx and NOx from marine exhaust gas by wet scrubbing method using urea peroxide solution. *Chemical Engineering Journal*, 390, 124567. https://doi.org/10.1016/j.cej.2020.124567
- Zhou, X., Li, T., Wang, N., Wang, X., Chen, R., & Li, S. (2022). Pilot diesel-ignited ammonia dual fuel low-speed marine engines: A comparative analysis of ammonia premixed and high-pressure spray combustion modes with CFD simulation. *Renewable and Sustainable Energy Reviews*, 173. https://doi.org/10.1016/j.rser.2022.113108
- Zincir, B. (2022). Environmental and economic evaluation of ammonia as a fuel for short-sea shipping: A case study. *International Journal of Hydrogen Energy*, 47(41), 18148–18168. https://doi.org/10.1016/j.ijhydene.2022.03.281
- Zincir, B., Shukla, P. C., & Agarwal, A. K. (2023, June). Decarbonization of maritime transport. Springer.

Appendix A

Simulink implementation and code

This Appendix shows the Simulink blocks as created for the simulation. The explanation and mathematical model are described in chapter 6.

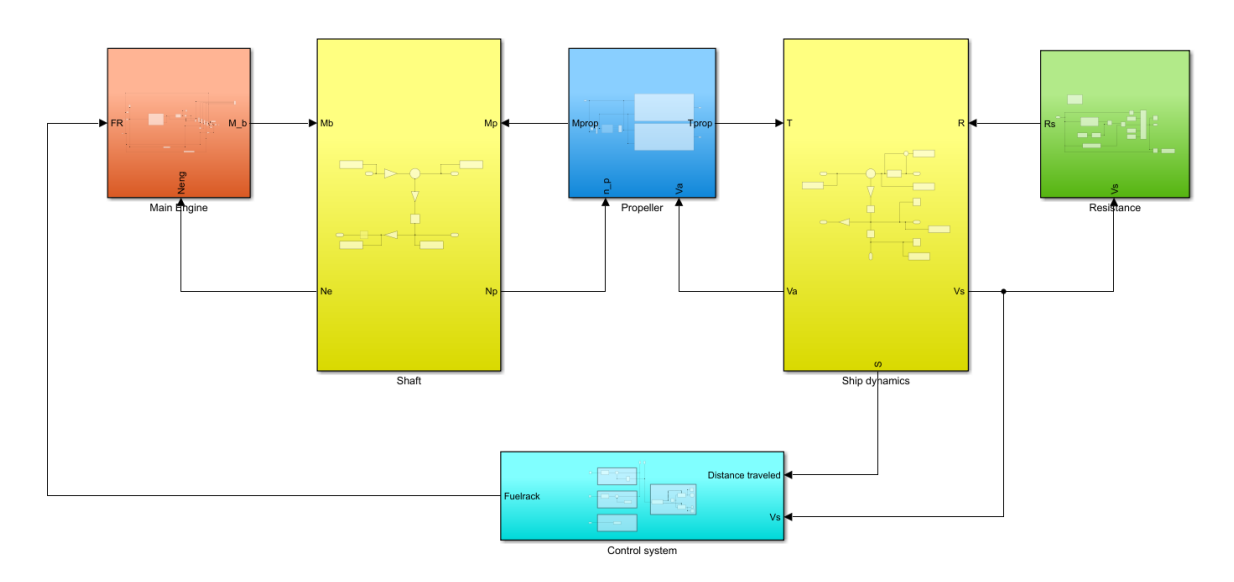


Figure A.1: Simulink model layout

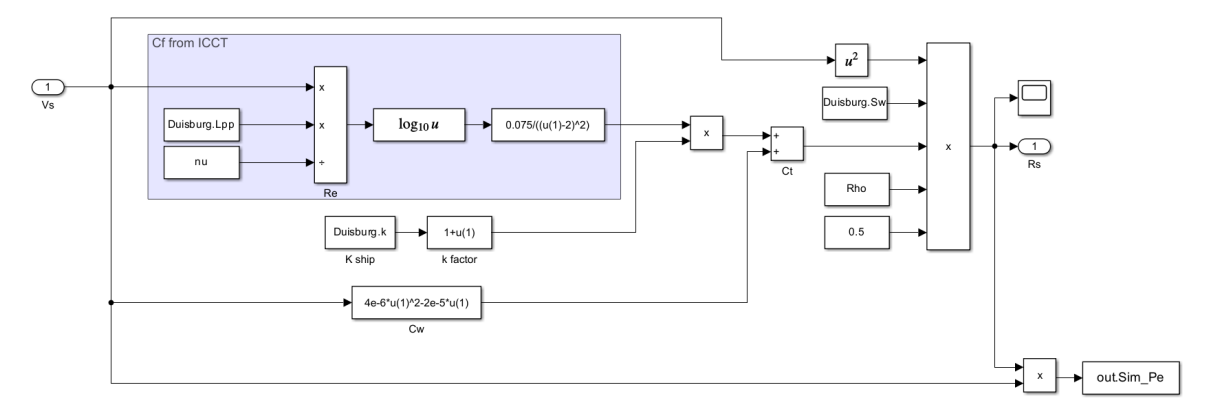


Figure A.2: Simulink Resistance block

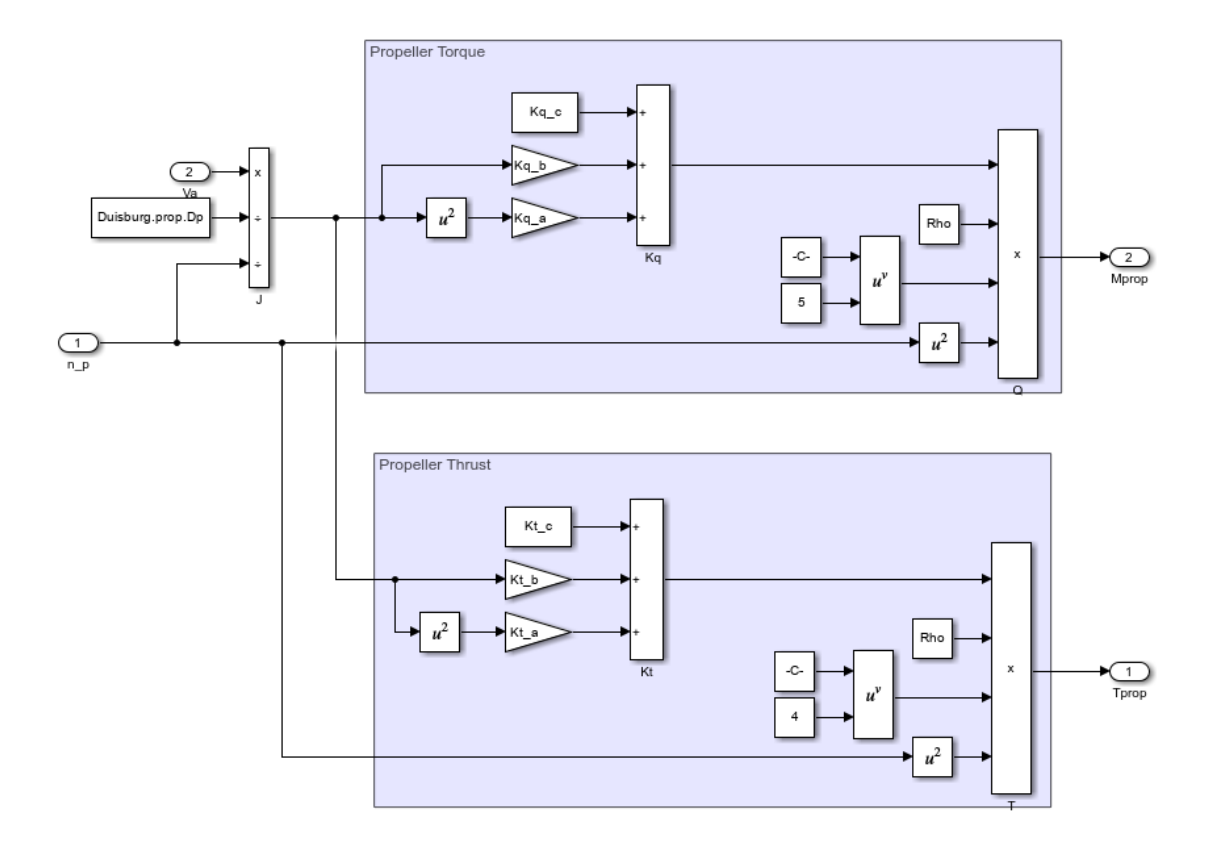


Figure A.3: Simulink propeller block

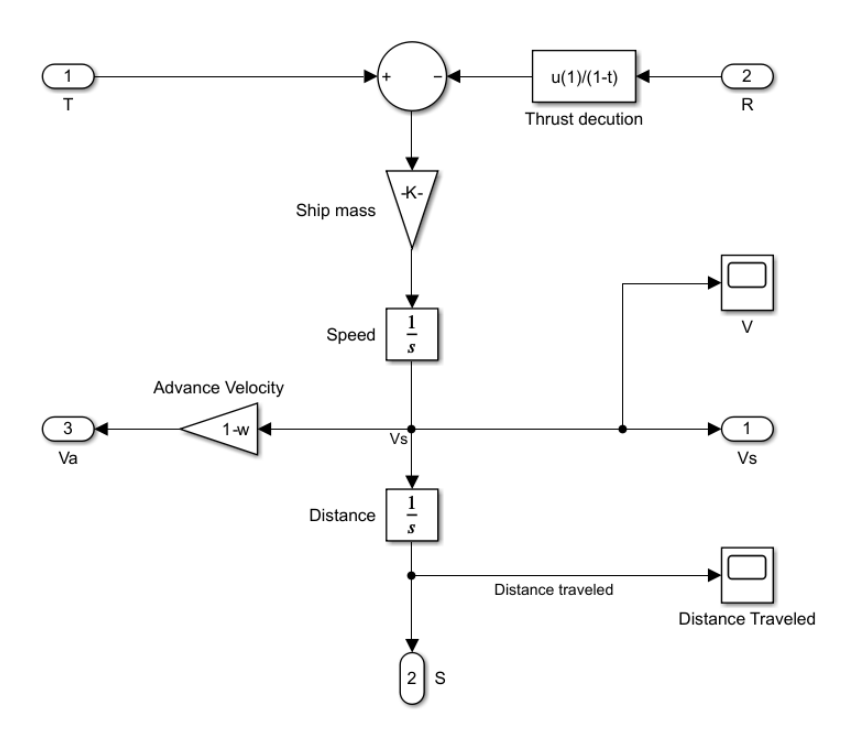


Figure A.4: Simulink Ship block

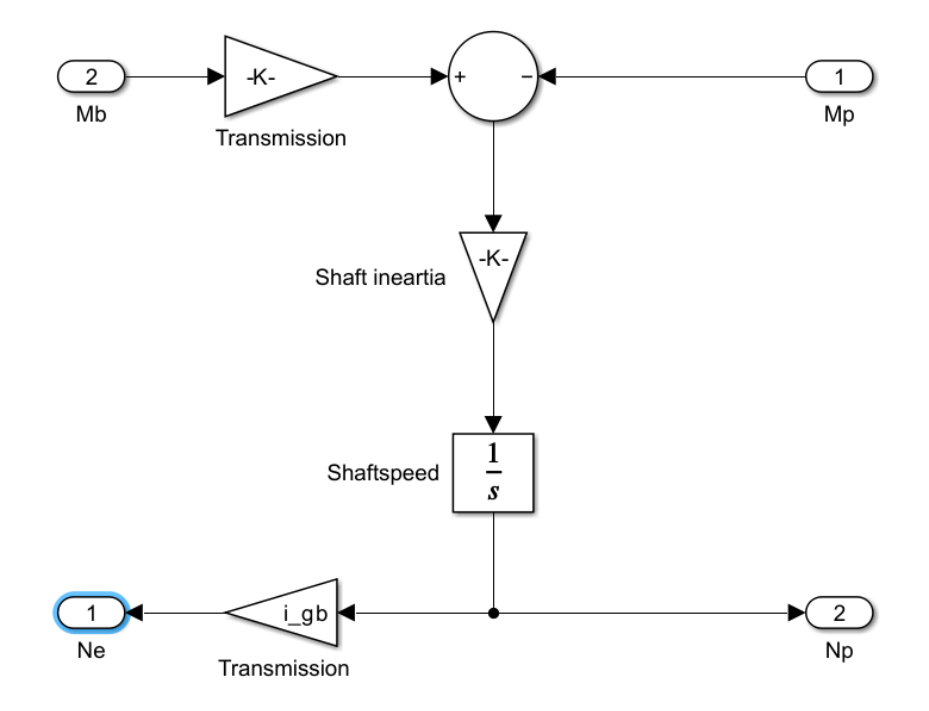


Figure A.5: Simulink Shaft block

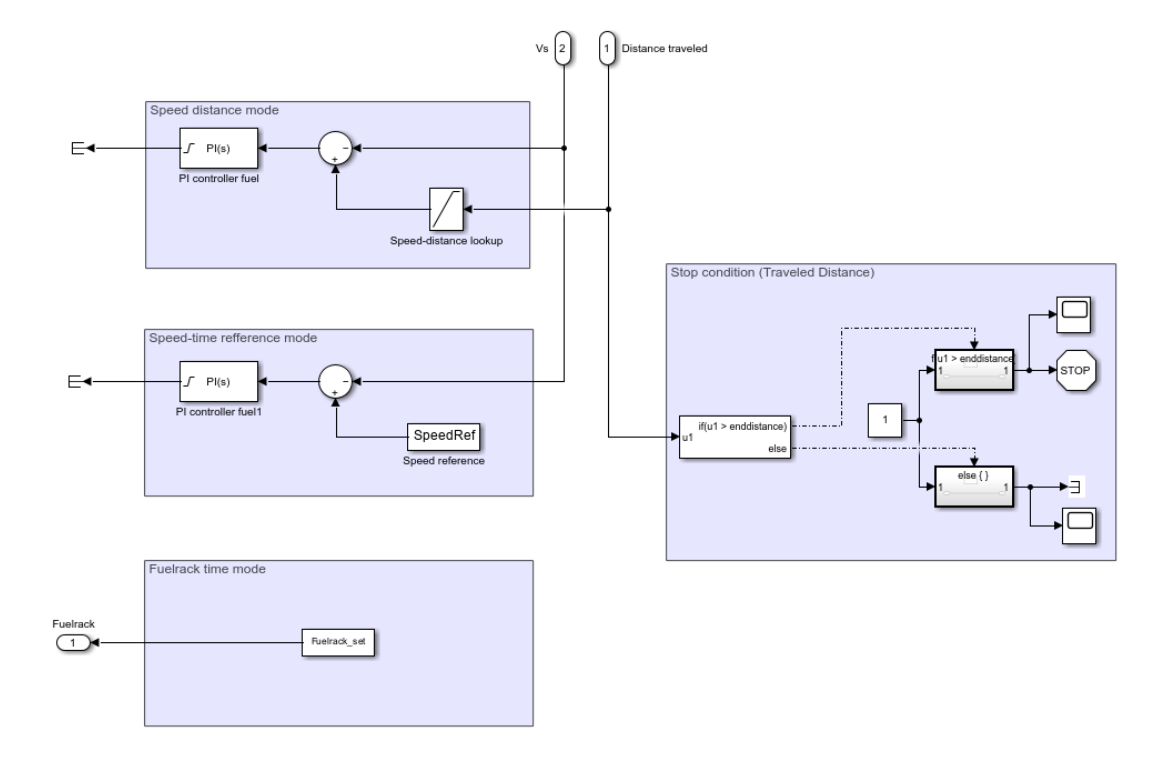


Figure A.6: Simulink control system

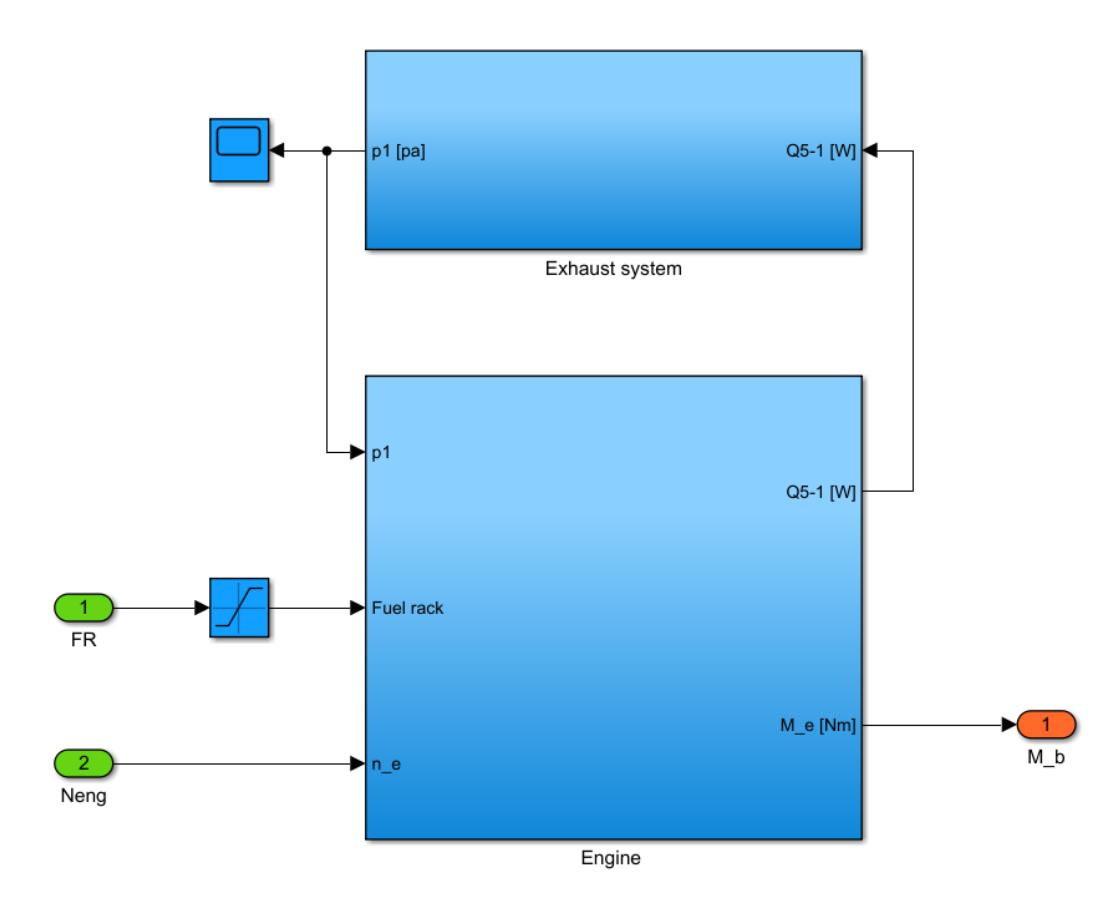


Figure A.7: Engine implementation in Simulink

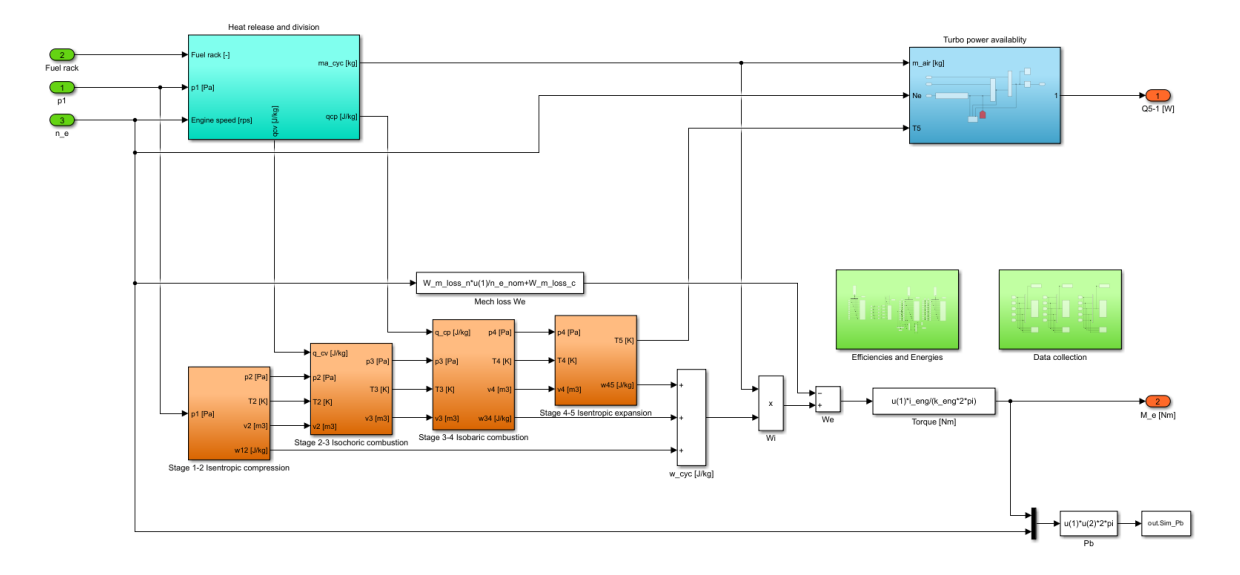


Figure A.8: Seiliger implementation in Simulink

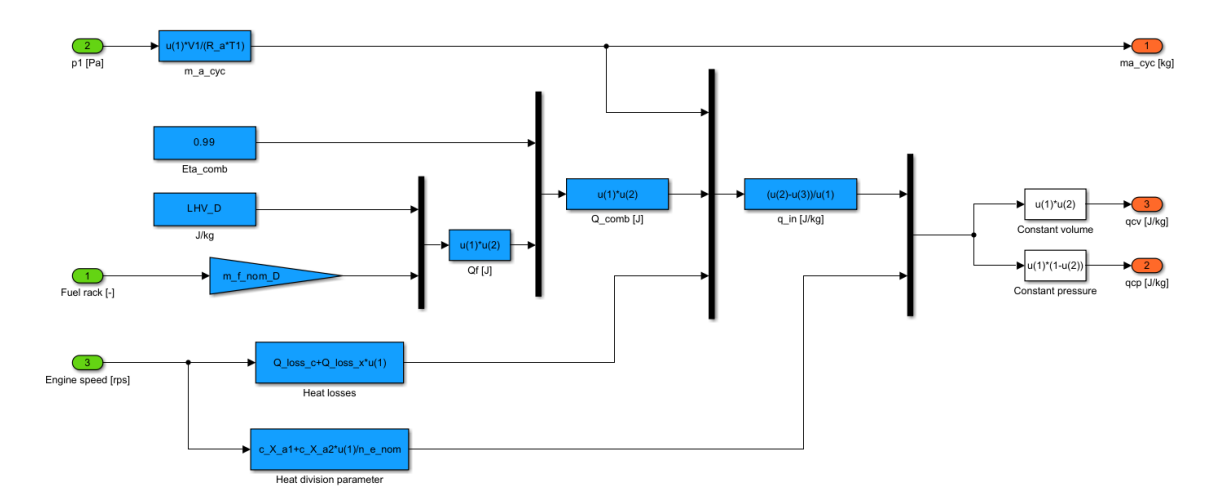


Figure A.9: Cylinder heat input model with heat input, combustion and cooling losses and heat division

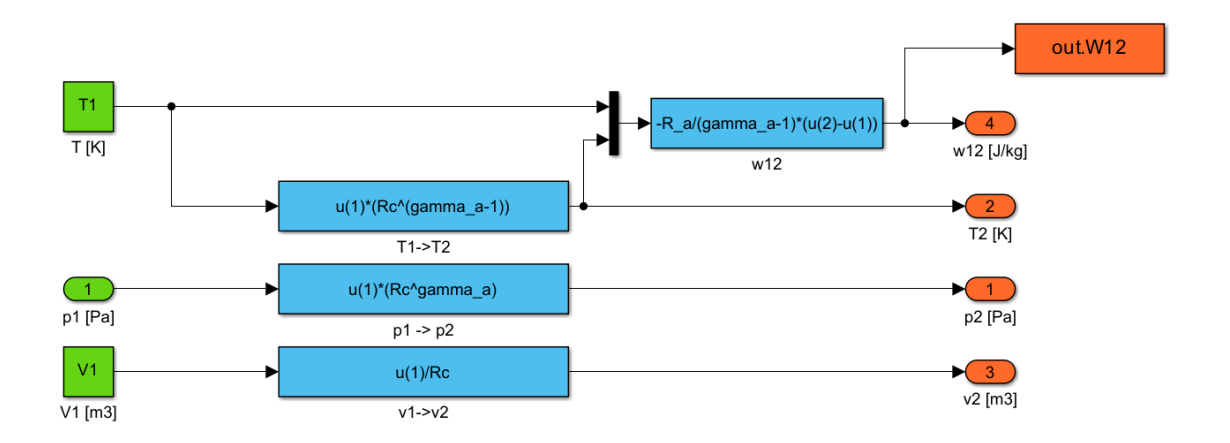


Figure A.10: Implementation of the thermodynamic formulas for isentropic compression

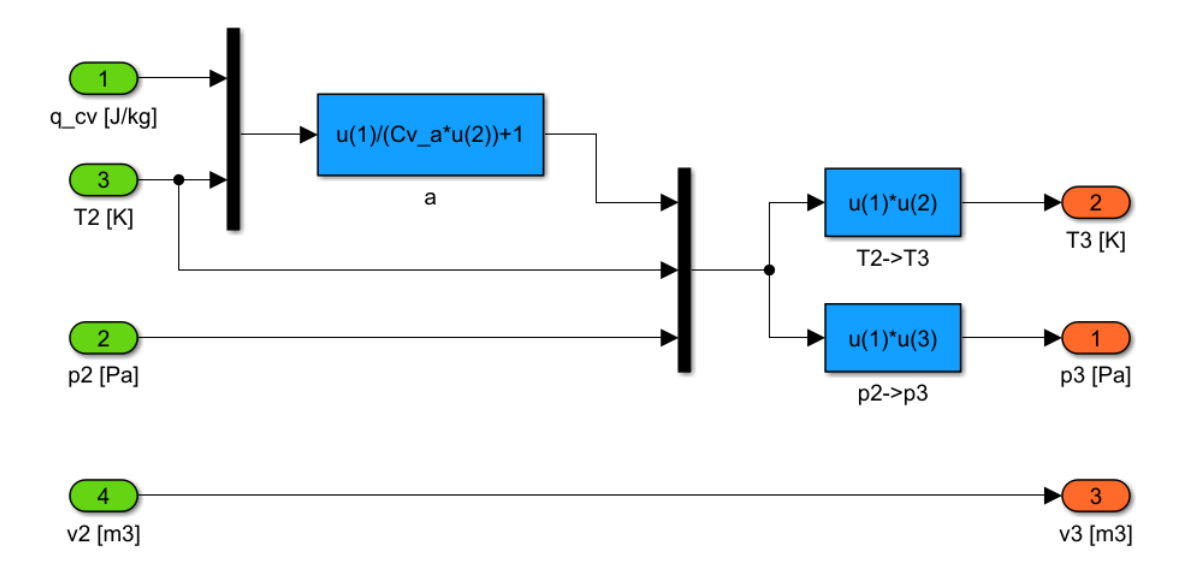


Figure A.11: Implementation of the thermodynamic formulas for isochoric combustion

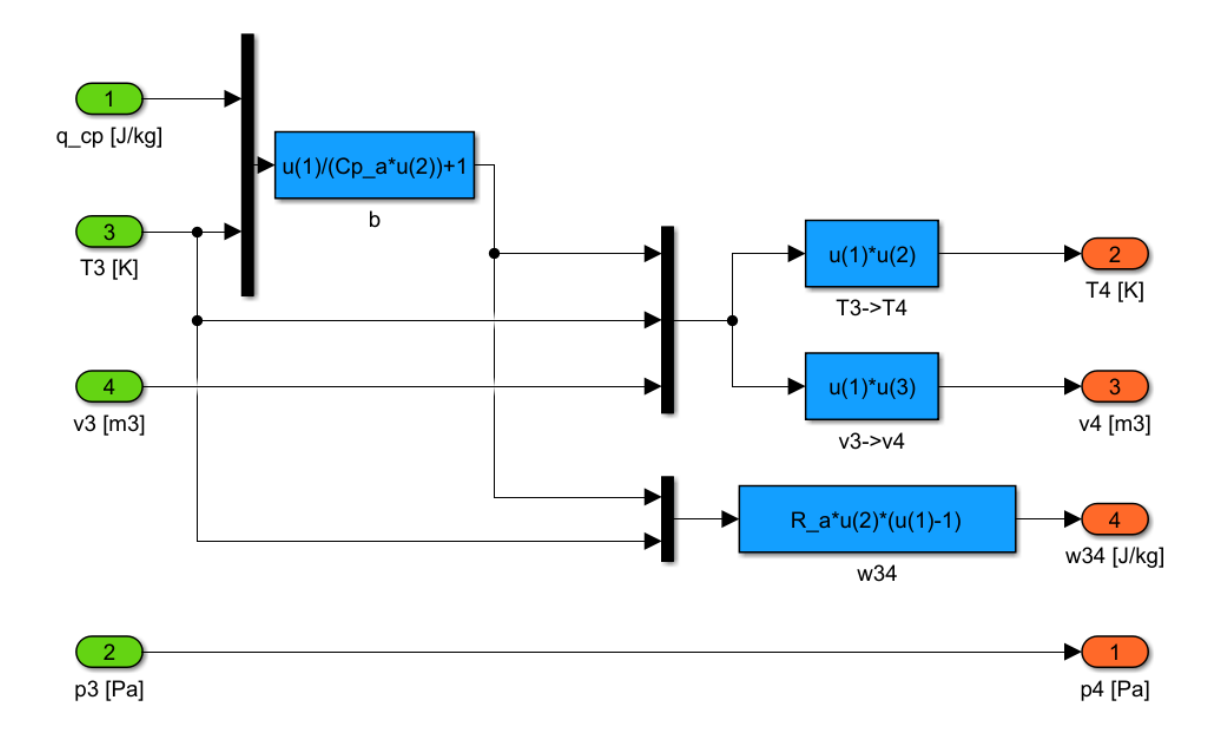


Figure A.12: Implementation of the thermodynamic formulas for isobaric combustion

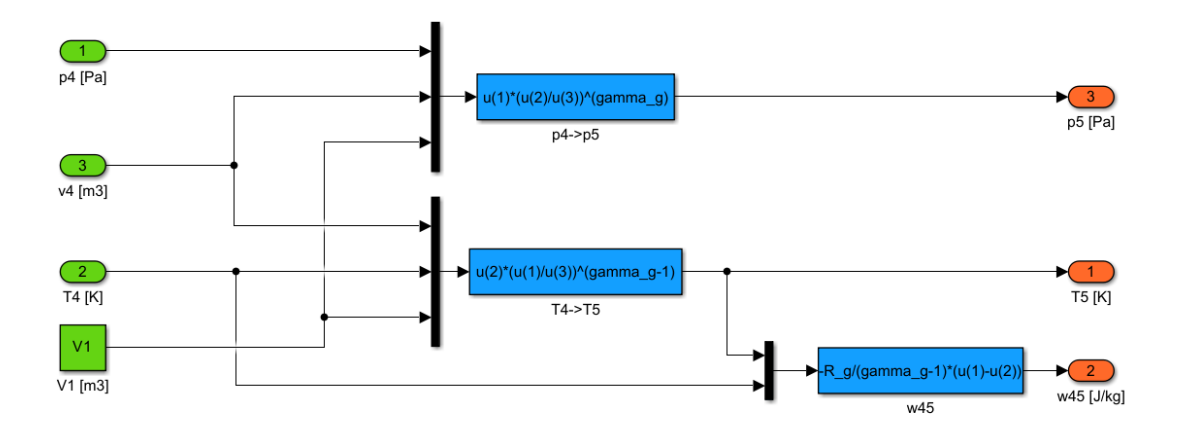


Figure A.13: Implementation of the thermodynamic formulas for isentropic expansion

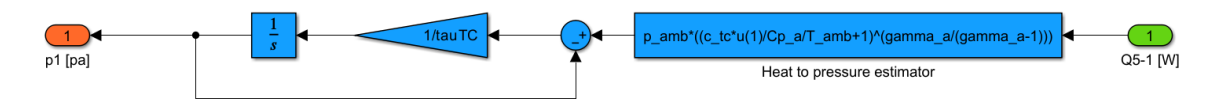


Figure A.14: Turbo model

Appendix B

Simulator Results

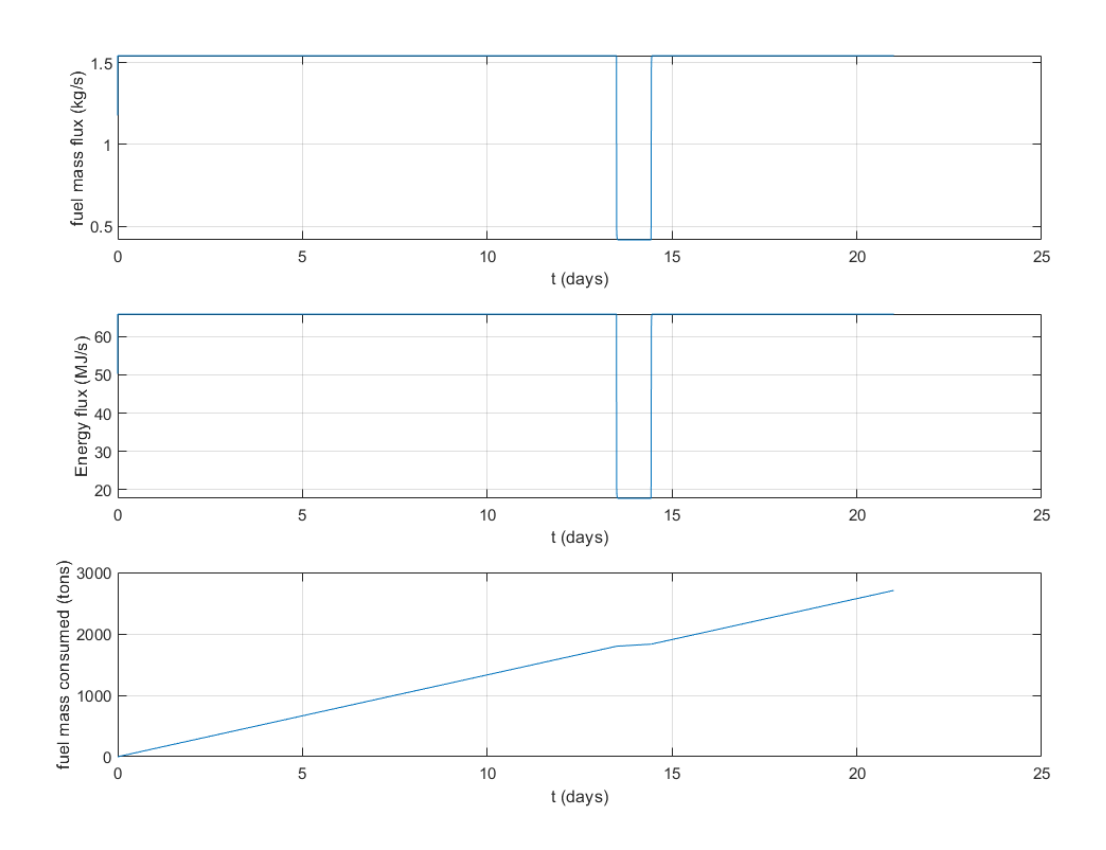


Figure B.1: Fuel mass flow, Energy flow and Fuel mass consumed for the Diesel voyage simulation

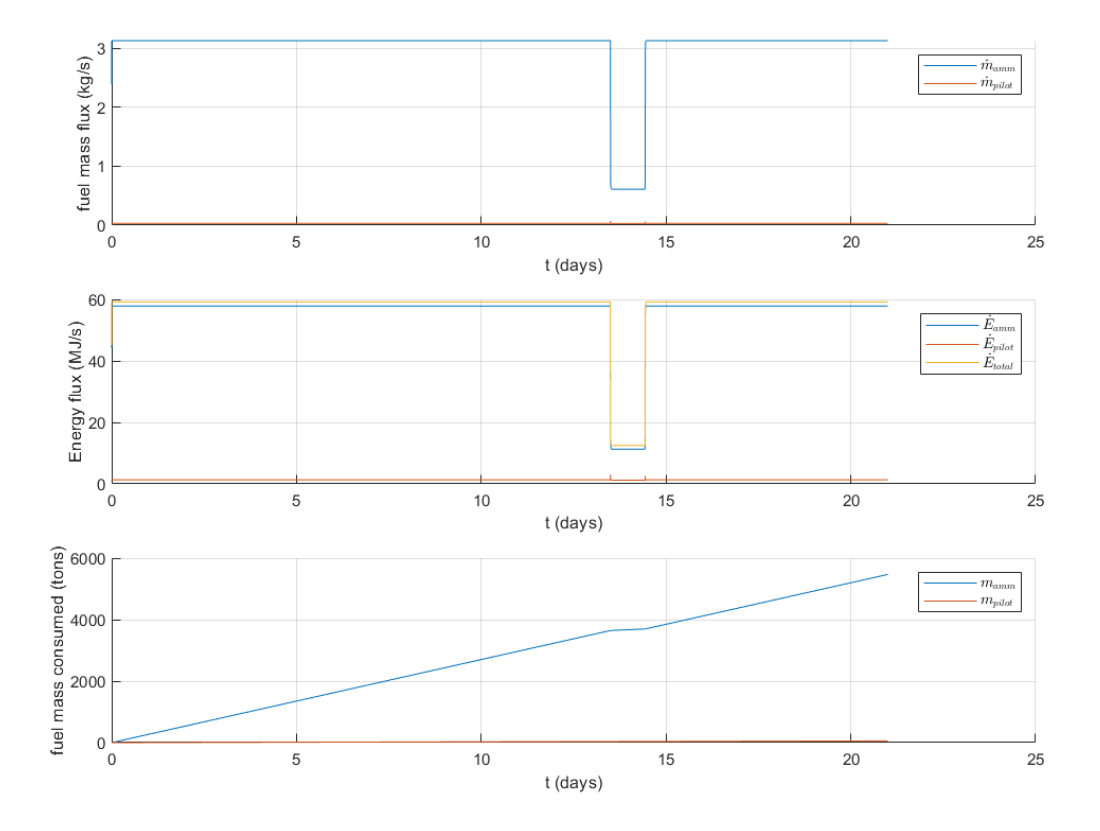


Figure B.2: Fuel mass flow, Energy flow and Fuel mass consumed for the Diesel-Ammonia voyage simulation

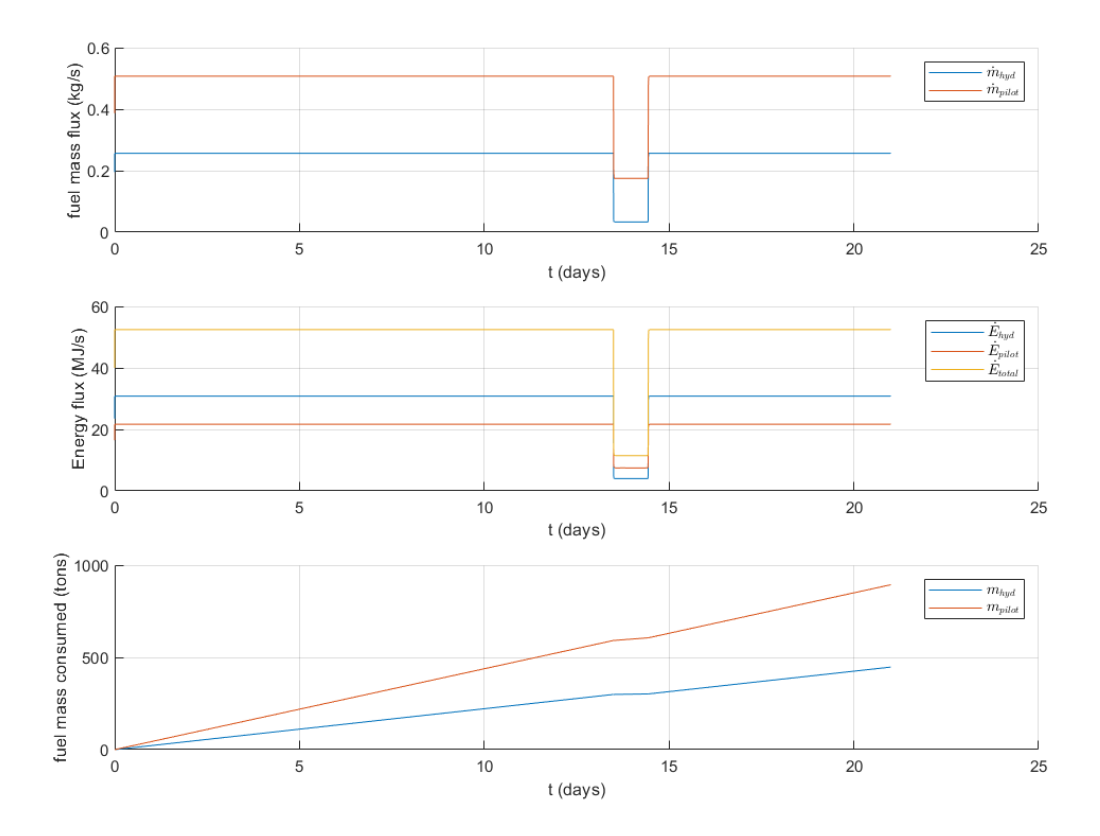


Figure B.3: Fuel mass flow, Energy flow and Fuel mass consumed for the Diesel-Hydrogen voyage simulation